Combustion and Flame 281 (2025) 114393

Contents lists available at ScienceDirect

Combustion and Flame

journal homepage: www.sciencedirect.com/journal/combustion-and-flame

Direct numerical simulation of nonpremixed ignition under gasoline compression-ignition engine conditions

Zisen Li [a,c,*], Evatt R. Hawkes [a], Armin Wehrfritz [b], Bruno Savard [c]

[a] School of Mechanical and Manufacturing Engineering, University of New South Wales, Sydney, NSW 2052, Australia
[b] Department of Mechanical and Materials Engineering, University of Turku, Turku 20014, Finland
[c] Department of Mechanical Engineering, Polytechnique Montréal, Montréal H3T 1J4, Canada

ARTICLE INFO

Keywords:
Direct numerical simulation
Gasoline compression-ignition engine
Primary reference fuel
Turbulent autoignition
Residence time

ABSTRACT

We present an analysis of the ignition process in thermochemical conditions relevant to gasoline compression-ignition (GCI) engines using direct numerical simulation (DNS). Two-dimensional DNS modelling the interaction of turbulence with an igniting double mixing layer are carried out. Three different primary reference fuel (PRF) blends, PRF0, PRF70, and PRF90, to span a range of different possible compression ignition scenarios are investigated. The fuel chemistry is shown to significantly affect the ignition process and the transition to a fully burning high-temperature flame. All three cases exhibit a diffusively supported cool flame which propagates towards richer mixtures faster than expected from homogeneous ignition delays. High-temperature combustion (HTC) initiates in rich mixtures in the PRF0 case, in both rich and lean mixtures in the PRF70 case, and in lean mixtures in the PRF90 case, which is consistent with expectations from homogeneous ignition delays. Budget analysis shows that HTC flames are diffusively supported in all cases, and as a result progress more rapidly from the ignition location to surrounding mixtures than homogeneous ignitions suggest. A quantitative model is proposed for the premixed flame propagation speed in the stratified and autoignitive mixtures. By considering the effects of normalised residence time of reactant at the flame surface, the conditional mean turbulent flame speed, conditioned upon mixture fraction, can be related to 1D referenced laminar flame speeds. The mechanism of consumption of the stoichiometric surface is examined by considering both displacement speed statistics and by tracking each single edge flame front. In the PRF0 case the results show the stoichiometric surface is consumed mostly by propagating HTC fronts that are almost parallel to it, which is referred to parallel consumption mode, while results in the PRF70 and PRF90 cases show signatures of edge-flame propagation as a secondary mechanism. For edge-flame mode the contribution of tangential-to Z diffusion to the displacement speed prevails over that of normal-to-Z diffusion. Overall the results demonstrate significant fuel-chemistry effects on the evolution of the ignitions, which will probably translate into significant differences in flame structure in a practical GCI engine.

Novelty and significance statement

This work presents the first DNS of turbulent, nonpremixed autoignition targeting fuel chemistry effects in gasoline compression ignition (GCI) engines. The novelty further arises from two aspects. First, it is the first study to quantitatively model flame displacement speed in autoignitive, stratified mixing layers using the residence time concept. Second, the evolution of edge flame fronts is tracked in complex turbulent flows to enable temporal characterisation of edge flame dynamics and reveal how tangential-to-mixture-fraction diffusion varies across different propagation modes. The significance lies in the implications for practical GCI engine design, as fuel chemistry significantly affects the flame structure, akin to how unravelling the diesel flame structure advanced engine design. These findings also highlight the need to improve practical CFD models, such as incorporating residence time into level-set-based approaches for accurate flame speeds, or characterising conditional fluctuations arising from mixed edge flame modes in flamelet or CMC models.

---

* Corresponding author at: School of Mechanical and Manufacturing Engineering, University of New South Wales, Sydney, NSW 2052, Australia.
E-mail address: zisen.li@polymtl.ca (Z. Li).

https://doi.org/10.1016/j.combustflame.2025.114393
Received 9 April 2025; Received in revised form 29 July 2025; Accepted 3 August 2025

1. Introduction

Increasing global concern over the need to limit greenhouse gas emissions, set against continuing needs to improve urban air quality, provides an imperative to develop more efficient and less polluting engines. Compression-ignition (CI) engines, which dominate the heavy-duty transport sector due to their high thermal efficiency and high energy density, face major challenges to further reduce emissions of soot and nitrogen oxides (NO_x), as required by the latest emission standards such as Euro-VI [1].

Gasoline compression-ignition (GCI) is a high-efficiency, low emissions engine concept wherein a low ignition quality fuel is employed in a CI engine [2–4]. By increasing the ignition delay and thus the level of premixedness, GCI engines can reduce the production of soot and NO_x are effectively suppressed. This strategy is similar to that adopted by homogeneous charge compression-ignition (HCCI) engines. GCI is distinguished from HCCI in a way that the fuel injection is sufficiently late so as to provide some control over ignition timing and combustion duration, but early enough to limit pollutant formation [5]. Based on the level of fuel/air stratification and premixedness, GCI engines can achieve a partially-premixed combustion mode that lies in between the fully premixed (HCCI engines) and nonpremixed (conventional diesel engines) combustion modes [5].

GCI has been shown to reduce emissions of soot and NO_x and keeps the high efficiency of CI engines in a series of both research [2,5–10] and commercial engine tests [11]. For example, GCI has demonstrated brake thermal efficiencies exceeding 50% [9,10,12], and engine-out emissions satisfying Euro-VI [1], which is impressive considering the amount of work to date. In the above works, gasoline-like fuel with research octane number (RON) ranging between 60 and 98 have been used, with the optimal RON number found to be in the range of 70–85 [5,7]. The progress so far has been achieved by engine performance tests, which do not provide a detailed understanding of how the combustion process of GCI differs from the more widely investigated combustion modes. The objective of this work is to begin to unpick these differences by using a series of representative direct numerical simulations (DNS). In reviewing previous works, both experimental and numerical studies (with a focus on DNS) are provided in terms of diesel combustion, due to its high relevance to GCI combustion.

Diesel fuels and their representative reference fuels exhibit two-stage ignitions, wherein a first, low-temperature chemistry (LTC) flame, or cool flame, precedes the main, high-temperature chemistry (HTC) ignition. The kinetics are described elsewhere, e.g., Refs. [13,14] and the references therein, but in brief the LTC phase results from H-abstraction from the fuel followed by a series of oxygen additions and isomerisations, resulting ultimately in the formation of ketohydroperoxides (KET), which break down producing radicals leading to chain branching and some heat release. However, after a certain critical temperature is reached, the oxygen addition reactions reverse direction leading to termination of the first stage. The products of the first stage, which include significant hydrogen peroxide (H_2O_2) and formaldhyde (CH_2O), then slowly proceed towards HTC ignition until another critical temperature is reached where H_2O_2 breaks down into two OH, resulting quickly in thermal runaway.

Most of our understanding of diesel-engine combustion has been obtained via experimental research on optically accessible engines and high-pressure combustion chambers [15–17]. An important contribution of this body of work is the so-called conceptual model of conventional diesel combustion [16], which informs a multi-stage and multi-mode ignition process consisting of two stages of ignition, and depicts the overall flame structure via the following process. First, after injection, the liquid fuel jet breaks up, evaporates into gaseous phase and mixes with the entrained air, forming a rich fuel/air mixture. Then the premixtures undergo the two-stage ignition driven by sequential LTC and then HTC combustion. The products of the rich premixed flame, and any residual fuel fragments or residual products of the first-stage ignition are mixed with air and burned in a diffusion flame that shrouds the jet. The flame structure informed by conceptual models was further corroborated by numerical studies including Reynolds-averaged Navier–Stokes simulation (RANS) [18] and large-eddy simulation (LES) [19].

Development of a conceptual model for GCI-engine combustion requires knowledge of the fundamental combustion processes in GCI conditions. While clarifying the overall structure, the experimental techniques used in diesel-engine conditions can only measure a few chemical species and have a very limited spatial resolution. On the other hand, RANS and LES, which have been performed to complement the experimental studies and further provide a sensitivity of the flame structure on parametric variations, are subject to modelling assumptions and limited flame details provided by the mean fields. An alternative method is given by direct numerical simulation (DNS), which resolves all relevant scales of turbulent motion and as a result provides a first-principles approach to turbulence-chemistry interaction.

DNS studies on ignition in turbulent stratified mixture have received considerable attention, as comprehensively reviewed by Mastorakos [20]. An early, seminal DNS study of single-stage nonpremixed ignitions in a two-dimensional (2D) mixing layer with a one-step chemistry model by Mastorakos et al. [21] identified that ignition occurs first in regions close to the most-reactive mixture fraction (Z_{mr}), which corresponds to the mixture having the shortest ignition delay time (τ_{mr}) in a homogeneous reactor. The same study also identified that regions of enhanced local mixing rate, as quantified by the scalar dissipation rate ($\chi = 2D(\nabla Z)^2$ where D is the diffusivity) in the current work, exhibited a longer ignition delay time relative to the homogeneous case. A similar ignition behaviour was observed in the ignition of a nonpremixed *n*-heptane flame where a global [22] or a four-step [23] reduced mechanism was used. It was also shown that the ignition started in the centre of vortical structures and evolves towards the vortex periphery where strain dominates. As DNS became computationally more affordable, and interest in alternative engine concepts diversified, later works have considered an array of different ignition scenarios, with different fuels, e.g., hydrogen [24–26], dimethyl ether (DME) [27–29], *n*-dodecane [30–32], and different setups representing different engine concepts, from conventional diesel combustion [31,33,34], HCCI [29,35], and reactivity controlled compression ignition (RCCI) [36], and others. Among these works, the works on conventional diesel combustion are the most relevant to the present study, and this is reviewed in the following.

Considering LTC, the situation for nonpremixed ignitions of two-stage ignition fuels differs from the one-step chemistry picture outlined by Mastorakos et al. [21]. Mukhopadhyay et al. [37] used one-dimensional simulations of the ignition of an *n*-heptane/air mixing layer to show that for sufficiently low dissipation rate, increasing χ could support the ignition of the stoichiometric region, but only up to a point wherein eventually further increases of χ resulted in delayed ignition. A later DNS study of the ignition of a two-dimensional DME/air mixing layer [27] showed that the cool flame is diffusively supported, and propagates more quickly into richer mixtures than homogeneous ignition delays would suggest, resulting in the much earlier appearance of high-temperature ignition kernels in these regions. Following HTC ignition, the authors showed that edge flames were formed, which had a tetrabrachial structure with the three conventional HTC branches (nonpremixed, lean, and rich premixed) attached to a preceding LTC branch, which was similar in structure to lifted laminar flames in the same conditions [33]. Later three-dimensional (3D) DNS studies in temporally evolving [27,31] and spatially evolving jets [28,38] confirmed many of the findings from 2D cases, and added new information on aspects such as the flow topologies where ignition was favoured [27], the local displacement speed of edge flames [27,31,38] and the flame stabilisation mechanism [28,38].

Compared to diesel, premixed flames are expected to play more important roles in GCI combustion due to the higher level of fuel/air mixing. In this context, flame propagation speed is likely to be affected by both premixture stratification and autoignition.

For the effect of stratification, Shi et al. [39] investigated the unsteady 1D laminar flame propagation in non-autoignitive n-C_7H_{16}/air with spatially varying equivalence ratio. They found that, when the stratification thickness (denoted by δ) is much larger than the flame thickness (δ_C), the stratified flame speed is highly correlated with the homogeneous flame speed (i.e., the nominal laminar flame speed of the local composition without stratification); as δ is reduced to the same level as δ_C, the stratified and homogeneous flame speeds differ more due to the preferential diffusion of H and OH radicals. Similar findings were made for premixed hydrogen [40] and methane [41] flames. Another work by Wang et al. [42] numerically investigated the speed of flame propagation along Z_{st} isosurface in a non-autoignitive DME/air counter-diffusion flow. It was found that the flame propagation speed along stoichiometry isosurface can be determined by the laminar flame speed of Z_{st} and the effect of curvature (or Markstein length), a feature typically exhibited by conventional premixed flames. These laminar results provide insights that the flame speed in the mixing layer, wherein the mixture fraction Z is stratified, can be modelled by the premixed flame speed of the corresponding homogeneous mixture of different Z.

For the effects of autoignition, Krisman et al. [27] showed that the premixed flame propagation speed increases with the residence time of the autoignitive reactant. Moreover, there exists a reference flame speed, S_C^{ref}, that demarcates the deflagrative and autoignitive flames. Such effect further complexes the prediction of flame propagation speed in autoignitive mixing layers. Mukhopadhyay and Abraham [37] proposed to estimate the flame propagation speed in autoignitive n-C_7H_{16}/air mixing layers based on the distance between Z_{st} and Z_{mr}, and the time that the ignition kernel propagates between these two sites. This strategy is similar to what was adopted for the autoignitive mixing layer case by Mastorakos et al. [21] wherein the physical distance between Z_{st} and Z_{mr} is estimated by $[D|Z_{\mathrm{st}} - Z_{\mathrm{mr}}|^2/\langle\chi|Z_{\mathrm{mr}}\rangle]^{0.5}$, which yielded a flame propagation speed about $0.5 \times S_C^{\mathrm{ref}}(Z = Z_{\mathrm{st}})$.

When the premixed flame arrives at and interacts with the stoichiometric isosurface, an edge flame structure may form. Due to its role in the stabilisation mechanism of lifted flames, the edge flame propagation speed, S_E, has received considerable attention in the literature. Previous studies revealed that S_E depends on multiple factors, including the level of micromixing [34,43–46], alignment between the reaction front and Z_{st} isosurface [27,31], edge-flame curvature [47,48], and upstream autoignition [28,33,49]. For instance, early DNS of a nonpremixed H_2 flame indicated that S_E decreases with χ. The negative correlation between S_E and χ was also observed in a 3D lifted H_2 nonpremixed flame, and found to be caused by the contribution of edge-flame curvature [46,50]. Under autoignitive diesel-engine conditions, Krisman et al. [34] also found that higher χ reduces the edge flame propagation speed by increasing its curvature and decreasing the premixedness ahead of the triple point. In a 3D n-heptane/air mixing layer [27], autoignition was found to produce a new scenario wherein the Z_{st} isosurface is consumed by an HTC reaction front which originates from spotty ignition kernels undergoing LTC and subsequently HTC ignition. In this case, the Z_{st} isosurface and HTC reaction front were highly aligned and S_E increased with χ.

The studies reviewed above considered atmospheric and conventional or low-temperature diesel combustion conditions. However, the situation may be quite different for conditions relevant to GCI, as a result of the differing fuel chemistry. At temperatures and pressures corresponding to the oxidiser conditions in a GCI engine, lean and stoichiometric *iso*-octane/air mixtures exhibit a single-stage high-temperature ignition with no preceding cool flame, and as will be shown the most-reactive mixture fraction is on the lean side, rather than the rich side as for n-heptane. Blends of *iso*-octane (i-C_8H_{18}) and n-heptane (n-C_7H_{16}) also have the potential to exhibit ignition and propagation behaviours that differ from the pure fuel conditions. Considering these potential differences, and to the authors' best knowledge the lack of any prior DNS of nonpremixed ignitions of PRF blends, the objective of the present work is to examine how nonpremixed ignitions and early flame development are affected by the PRF chemistry. The presented analysis will describe the structural transitions of the ignitions, the model for premixed flame propagation in the autoignitive mixing layer, and the mechanisms by which the stoichiometric isosurface is ignited.

The rest of the work is organised as follows. Section 2 introduces numerical methods. Results and discussions are provided in Section 3. A conclusion and an outlook are presented in Section 4.

2. Numerical methods

The DNS case setup is introduced in Section 2.1. The definition of progress variable and its displacement speed is presented in Section 2.2. The effect of autoignition on the flame displacement speed is illustrated by 1D premixed flames in Section 2.3. Finally the decomposition method for diffusion component of the flame displacement speed is presented in Section 2.4.

2.1. Case setup

Fig. 1 shows the configuration of the DNS setup for the PRF0 case. The PRF70 and PRF90 cases share the same configuration, differing only in the initial turbulence intensity (u') and fuel composition. The configuration adopted is similar to a previous series of DNS modelling the ignition of 2D double mixing layers with n-dodecane as fuel [30]. This configuration was selected as the simplest unit problem capable of exposing the influence of an unsteady turbulent flow on the ignition behaviour. A relatively cold, fuel-rich region is surrounded by a hot oxidiser region, and allowed to ignite under the influence of an imposed 2D synthetic turbulence field. The computational domain is $[0, 3.6] \times [-3.6, 3.6]$ mm in size, consisting of a periodic direction, x, and a transverse direction across the mixing layer, y, with non-reflecting outflow boundary conditions. The initial conditions are specified as a function of mixture fraction, Z, assuming adiabatic mixing between the pure fuel and oxidiser streams. The pure fuel stream ($Z = 1$) contains a mixture of n-C_7H_{16} and i-C_8H_{18} with a temperature computed from the enthalpy of the liquid fuel at 403 K, thus accounting for the latent heat of evaporation.[1] The oxidiser stream ($Z = 0$) corresponds to air approximated as 21 % oxygen and 79 % nitrogen by volume and a temperature of 1100 K is chosen for all cases. The stoichiometric mixture fraction, Z_{st}, is 0.062 for all three PRF blends. The initial pressure is 60 atm. These thermochemical conditions were chosen to be representative of GCI spray combustion experiments in the UNSW constant volume combustion chamber [51]. The initial mixture fraction profile is specified as $Z(y) = Z_0 \exp(-y^2/2\delta^2)$, where δ is the mixing layer thickness set to 100 μm unless specified otherwise; Z_0 is the centreline mixture fraction, which is set to 0.3 to account for premixing between fuel and air prior to the gaseous ignition.

A Passot–Pouquet turbulence spectrum is used to generate an initial 2D velocity field with a zero bulk velocity. (The 2D assumption is acknowledged as a limitation. It is necessary here due to the high pressure which imposes very short length scales and time-steps, and hence computational cost.) The spectrum is parameterised to render the initial Damköhler number ($Da = \tau_E/\tau_{\mathrm{mr}}$) equal to 0.3, a value lying in the range $Da = 0.1$–1 suggested by Pei et al. [18], characterising the conditions at the ignition location in diesel engines. Similar values

---

[1] The pure fuel stream hence has a temperature which is not physically realistic, however as mentioned later in this paragraph, the peak centreline mixture fraction is 0.3, so that pure fuel mixtures do not occur in the DNS.

Table 1
Initial turbulence ($Da = 0.3$) and reference flame parameters.

Reference parameters	PRF0	PRF70	PRF90
Initial turbulent fluctuation u' [m/s]	1.28	0.58	0.45
Minimum (or most reactive) 0D ignition delay τ_{mr} [ms]	0.25	0.57	0.73
Mixture fraction of minimum ignition delay Z_{mr}	0.125	0.145	0.032
Mixture fraction of second minimum ignition delay Z'_{mr}	–	0.03	0.19
Mixture fraction of lower bound of LTC, Z_C	0.08	0.11	0.13
Stoichiometric mixture fraction Z_{st}	0.062	0.062	0.062
Reference 1D flame displacement speed $S_C^{\mathrm{ref}}(Z_{\mathrm{st}})$ [m/s]	3.9	3.0	2.8

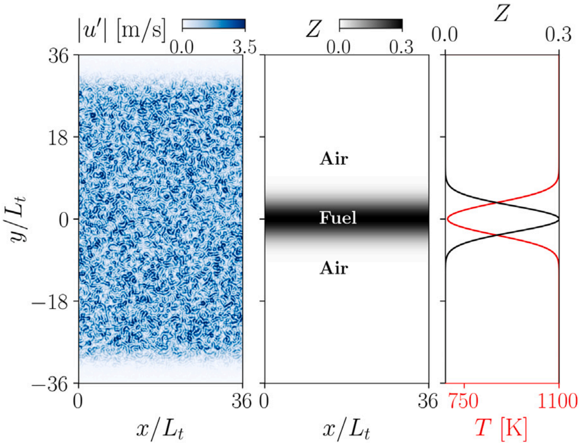

Fig. 1. Case setup and initial conditions for the PRF0 case, similar to PRF70 and PRF90. Left: contour of velocity magnitude $|\boldsymbol{u}'|$; middle: contour of mixture fraction Z; right: profile of mixture fraction (black solid line) and temperature T (red solid line) across the mixing layer. (For interpretation of the references to colour in this figure legend, the reader is referred to the web version of this article.)

have been employed in previous studies [27,30]. The turbulence time scale, $\tau_E = L_t/u'$, is set by fixing the integral length L_t to 0.1 mm for all three PRF cases and adjusting the characteristic turbulent velocity fluctuations u' to yield the target $Da = 0.3$. The chemistry time scale τ_{mr} corresponds to the most reactive ignition delay of each PRF fuel, as introduced shortly. A 116-species reduced chemical mechanism for PRF blends, including LTC and HTC pathways, is used [52]. The key parameters of the simulation setup are summarised in Table 1.

The governing equations for the conservation of mass, momentum, total energy and species mass fractions are solved for compressible, multicomponent reactive flows with detailed chemistry by S3D [53]. A 2D structured Cartesian mesh with size $\Delta x = \Delta y = 1\,\mu\mathrm{m}$ is adopted. Spatial differentiation is achieved through 8th-order finite differences [54]. Aliasing errors in the convective derivatives is reduced by re-formulating these terms in a skew-symmetric form as discussed in Ref. [55]. A 10th-order filter is applied to damp high-wavenumber oscillations. Time advancement is achieved through a 6-stage, 4th-order explicit Runge—Kutta method [56], avoiding the expensive all-to-all communication required in implicit methods.

The 2D DNS are complemented by zero-dimensional (0D) constant pressure homogeneous ignition calculations over the relevant mixture fraction range, and 1D laminar simulations. In the 0D homogeneous reactor calculations, ignition delay time ($\tau_{\mathrm{HTC}}^{\mathrm{0D}}$) is identified by the maximum heat release rate at a given mixture composition (i.e., Z value), and thus denotes the onset of HTC combustion and thermal runaway. The change of $\tau_{\mathrm{HTC}}^{\mathrm{0D}}$ over Z for each PRF case is plotted by the red line in Fig. 2a. The most-reactive ignition delay time (τ_{mr}) is then defined as the shortest ignition delay time over the entire mixture fraction range, i.e., $\tau_{\mathrm{mr}} = \min(\tau_{\mathrm{HTC}}^{\mathrm{0D}})$, thus corresponding to the most reactive mixture fraction, Z_{mr}, for each PRF blend. For PRF70 and 90, a second local minimum of $\tau_{\mathrm{HTC}}^{\mathrm{0D}}$ appears and the corresponding mixture fraction is denoted as Z'_{mr}. For cases undergoing two-stage ignition, the first-stage ignition delay time ($\tau_{\mathrm{LTC}}^{\mathrm{0D}}$) is defined as the time of the maximum consumption rate of ketohydroperoxide ($\dot{\omega}_{\mathrm{KET}}$), a marker for the onset of LTC reactions.

Table 2
Definition of high- (HTC) and low-temperature chemistry (LTC) combustion.

	Definition	Numerical identification
HTC ignition/flame	Peak HRR	$C = 0.85$
LTC ignition/flame	Peak $\dot{\omega}_{\mathrm{KET}}$	$C = 0.1 \cap Z > Z_C$

Two types of 1D laminar simulations are performed to aid the 2D turbulent analysis. The first is 1D mixing layer with initial conditions corresponding to the mixture profiles in the inhomogeneous direction of the 2D simulations. The mixing thickness is varied to investigate the effect of molecular mixing. The second is 1D premixed flame with the inlet corresponding to mixtures across the mixing layer. This will be introduced in more details in Section 2.3.

It should be noted that in the present case, the simulation time, t, can be also used as the fluid residence time and its distribution is spatially uniform. However, this no longer holds true for more general cases, e.g., 3D spatially developing jet, where the residence time needs to be solved [57] and its spatial gradient is non-zero. In the following discussion, two different normalised times are used: (1) $t^* = t/\tau_{\mathrm{mr}}$, denoted as "normalised time", is used for describing transient ignition process in Sections 3.1–3.5, and (2) $\tau^* = t/\tau_{\mathrm{HTC}}^{\mathrm{0D}}(Z)$, denoted as "normalised residence time", to characterise the effects of autoignition on flame propagation in Sections 2.3 and 3.6. Also note that the t^* and τ^* can be mutually converted by a factor of $\tau_{\mathrm{mr}}/\tau_{\mathrm{HTC}}^{\mathrm{0D}}(Z)$.

2.2. Definition of progress variable and displacement speed

To quantitatively measure the ignition delay, and to characterise the overall ignition process consistently for 0/1/2D results of all three PRF cases, a normalised progress variable, $C = \mathcal{Y}/\mathcal{Y}_{\mathrm{eq}}$ is defined. Here $\mathcal{Y} = 1 - \left(Y_{n\mathrm{C_7H_{16}}} + Y_{i\mathrm{C_8H_{18}}} + Y_{\mathrm{O_2}} + Y_{\mathrm{N_2}}\right)$, is the sum of the mass fraction of all chemical species except the reactants. Then $\mathcal{Y}$ is normalised by its constant-pressure equilibrium value obtained as a function of mixture fraction, $\mathcal{Y}_{\mathrm{eq}}(Z)$, to account for the stratification effect. It is found that the condition $C = 0.85$ agrees well with the local HRR peak for all 0/1/2D cases and PRF blends, and thus is used to numerically identify HTC combustion. Similarly the condition $C = 0.1$ combined with ($\cap$) $Z > Z_C$ agrees well with local $\dot{\omega}_{\mathrm{KET}}$ consumption peak and is used for identifying LTC combustion. For LTC, Z_C corresponds to the leanest mixture that can produce 5% of the maximum Y_{KET} in 0D reactors, and is used to rule out the single-stage ignition in fuel-lean regions. The definitions and numerical identification criteria of HTC and LTC ignition and flame are summarised in Table 2. The performance of the criteria can be referred to animations provided in Supplementary Material which illustrates the evolution of several key fields.

To quantify the speed at which the reaction fronts propagate and how this is affected by turbulence, we will analyse the displacement speed, which measures the propagating speed of an isosurface (e.g., $C = 0.85$) relative to the fluid, and is defined as

$$S_C = \frac{1}{|\nabla C|}\frac{\mathrm{D}C}{\mathrm{D}t}$$

$$= \frac{1}{|\nabla C|}\left(\frac{\partial C}{\partial \mathcal{Y}}\frac{\mathrm{D}\mathcal{Y}}{\mathrm{D}t} + \frac{\partial C}{\partial Z}\frac{\mathrm{D}Z}{\mathrm{D}t}\right)$$
$$= \frac{1}{|\nabla C|}\left(\frac{1}{\mathcal{Y}_{\mathrm{eq}}}\frac{\mathrm{D}\mathcal{Y}}{\mathrm{D}t} - \frac{\mathcal{Y}'_{\mathrm{eq}}(Z)\mathcal{Y}}{\mathcal{Y}^2_{\mathrm{eq}}(Z)}\frac{\mathrm{D}Z}{\mathrm{D}t}\right), \tag{1}$$

In the above equation, the total derivative ($\mathrm{D}/\mathrm{D}t$) for the normalised progress variable ($\mathrm{D}C/\mathrm{D}t$) is further split into contributions due to the evolution of the non-normalised progress variable, $\mathcal{Y}$, and mixture fraction Z. Their total derivatives read

$$\frac{\mathrm{D}\mathcal{Y}}{\mathrm{D}t} = \frac{\mathrm{D}}{\mathrm{D}t}\mathcal{L}_{\mathcal{Y}}[\boldsymbol{Y}]$$
$$= \mathcal{L}_{\mathcal{Y}}\left[\frac{\mathrm{D}\boldsymbol{Y}}{\mathrm{D}t}\right]$$
$$= \underbrace{\sum_{k=1}^{N_{\mathrm{sp}}}\alpha_{\mathcal{Y},k}\left[\frac{1}{\rho}\nabla\cdot\left(\rho D_k\left(\nabla Y_k + Y_k\frac{\nabla W}{W}\right)\right)\right]}_{\mathrm{diff.}} + \underbrace{\sum_{k=1}^{N_{\mathrm{sp}}}\alpha_{\mathcal{Y},k}\dot{\omega}_k}_{\mathrm{react.}}, \tag{2}$$

and

$$\frac{\mathrm{D}Z}{\mathrm{D}t} = \frac{\mathrm{D}}{\mathrm{D}t}\mathcal{L}_Z[\boldsymbol{Y}]$$
$$= \sum_{k=1}^{N_{\mathrm{sp}}}\alpha_{Z,k}\left[\frac{1}{\rho}\nabla\cdot\left(\rho D_k\left(\nabla Y_k + Y_k\frac{\nabla W}{W}\right)\right)\right], \tag{3}$$

where $\mathcal{L}_{\mathcal{Y}}(\boldsymbol{Y}) = \sum_k \alpha_{\mathcal{Y},k}Y_k$ and $\mathcal{L}_Z(Y_k) = \sum_k \alpha_{Z,k}Y_k$ denote the weighted linear sum of mass fractions Y_k to $\mathcal{Y}$ and Z, respectively. Here the mixture fraction is calculated according to Bilger's definition [58]. The diffusion and reaction components of S_C are denoted as $S_{C,\mathrm{d}}$ and $S_{C,\mathrm{r}}$, respectively. These two terms are calculated by using the corresponding part in the $\mathrm{D}\mathcal{Y}/\mathrm{D}t$ term, i.e., $S_{C,\mathrm{d}} = \frac{1}{|\nabla C|\mathcal{Y}_{\mathrm{eq}}}[\mathrm{diff.}]$ and $S_{C,\mathrm{r}} = \frac{1}{|\nabla C|\mathcal{Y}_{\mathrm{eq}}}[\mathrm{react.}]$, which will be used later in examining the propagation mechanism of the reaction fronts.

2.3. Effects of autoignition and residence time

In the present case the premixtures are highly autoignitive. As a result the flame propagation speed is expected to be significantly affected by the residence time of the reactant, which measures for how long time the reactant has autoignited before it enters the flame, as shown by Krisman et al. [59]. The flame propagation speed would be significantly enhanced if the residence time of the reactant approaches its ignition delay time [60]. Here the dependence of flame propagation speed on the residence time of the reactant is estimated by 1D premixed flames, with their inlet condition corresponding to the mixtures across the mixing layer. Fig. 2b-d gives an example for $Z = 0.12$ of the PRF0 case. A series of 1D premixed flames with varying inlet velocities are performed with Cantera [61]. The inlet composition and temperature are specified as those of the 2D initial condition with the corresponding Z. Each 1D flame can be characterised by a residence time

$$t = \int_0^{x_{\mathrm{f}}}\frac{1}{u(x)}\mathrm{d}x, \tag{4}$$

where x, $u(x)$ and x_{f} denote the spatial coordinate, flow velocity field and flame position, respectively. We choose x_{f} to be where $C = 0.85$ (as shown by the dots in Fig. 2a). The flame propagation speed can be characterised by the displacement speed $S_C = S_C(C = 0.85)$. In the 1D simulation, the reactant residence time t can be increased by increasing the inlet flow velocity, which is numerically achieved in Cantera by prolonging the domain length (note that the flame location is fixed approximately at the domain centre). Fig. 2b and c show the distribution of C in x space and the change of flame location x_{f} over flame displacement speed S_C, respectively. When the residence time of the reactant is much lower compared to the ignition delay time (e.g, $\tau^* < 0.2$), the flame is stabilised at the inlet, as shown by the grey solid lines near $x = 0$ in Fig. 2b or grey dots in Fig. 2c. In this case, the autoignition is limited due to the short residence time of reactants and as a result the flame is dominantly stabilised by diffusion. As the inlet velocity increases and the residence time becomes comparable to the ignition delay (e.g., $\tau^* > 0.4$), the flame is lifted away from the inlet and S_C is enhanced significantly due to autoignition. Such transition from diffusion- to autoignition-driven stabilisation is highlighted by the coloured lines ranging from blue to red. As the inlet velocity becomes very large, flame stabilisation is dominantly governed by autoignition, with the limit corresponding to the 0D solution with time mapped onto residence time t (Eq. (4)) in Fig. 2b. The referenced flame speed, S_C^{ref}, which demarcates the diffusion and autoignition regime, can be taken of yielding the maximum derivative $\mathrm{d}x_{\mathrm{f}}/\mathrm{d}S_C$ (vertical blue dashed line in Fig. 2c). The flames with $S_C < S_C^{\mathrm{ref}}$ are deflagrations while those with $S_C > S_C^{\mathrm{ref}}$ are autoignitions. As expected, the derivative $\mathrm{d}x_{\mathrm{f}}/\mathrm{d}S_C$ approaches the ignition delay (≈ 0.25 ms) as $\tau^* \to 1$. The referenced 1D premixed flame speed of the stoichiometric mixture, $S_C^{\mathrm{ref}}(Z_{\mathrm{st}})$, for each PRF case is listed in Table 1.

Based on the S_C and S_C^{ref}, an acceleration factor Λ is defined as their ratio, $\Lambda = S_C/S_C^{\mathrm{ref}}$, which is a function of the normalised residence time, $\tau^* = t/\tau^{\mathrm{0D}}_{\mathrm{HTC}}(Z)$. It can be seen from Fig. 2c that Λ increases exponentially as τ^* approaches 1 (albeit Λ never reaches 1). The value of Λ is then tabulated as a function of Z and τ^*. In this procedure, we noted that numerical issues may emerge due to the interpolation based on the irregular $Z - \tau^*$ coordinate. To alleviate this issue, the dependence of $\Lambda = S_C/S_C^{\mathrm{ref}}$ on τ^* is fit to an analytical function for each Z. Here we choose the model of S_C/S_C^{ref} proposed by Zhang and Ju [60] for pure premixed flames. The model is given by the following form

$$\frac{S_C}{S_C^{\mathrm{ref}}} = \sqrt{\frac{T_{\mathrm{f}} - T_0}{T_{\mathrm{f}} - T_{\mathrm{p}}}}. \tag{5}$$

In Eq. (5), T_{f} and T_0 denote the peak and unburned flame temperature and are available from 1D simulation; T_{p} is a critical temperature that demarcates the autoignition and deflagration regime within the flame, and can be obtained by solving the following equation

$$\tau^*\int_{T_0}^{T_{\mathrm{a}}} T^{-b}\exp\left(\frac{T_{\mathrm{a}}}{T}\right)\mathrm{d}T = \int_{T_0}^{T_{\mathrm{p}}} T^{-b}\exp\left(\frac{T_{\mathrm{a}}}{T}\right)\mathrm{d}T, \tag{6}$$

where T_{a} and b are activation temperature and a constant, respectively. In the original work by Zhang and Ju [60], T_{a} can be estimated based on homogeneous ignition with one-step mechanism and b is a free parameter. In the present work, T_{a} is chosen to be the 1D flame temperature of $C = 0.85$ and b is fitted according to 1D results for each Z. Fig. 2a shows the contour of Λ in $Z - t$ space. The result of Λ for PRF0, $Z = 0.12$ is also plotted in Fig. 2d to demonstrate the performance of Eq. (5). Consistent with $Z = 0.12$, for all Z the value of Λ increases significantly as the residence time t approaches $\tau^{\mathrm{0D}}_{\mathrm{HTC}}$ (or equivalently, the normalised residence time τ^* approaches 1). The values of Λ can be tabulated as a function of (Z, τ^*), and its purpose is to give an estimate of flame displacement speed enhancement by autoignition compared to the reference deflagrative speed as the flame passes a premixture of Z with normalised residence time τ^*.

2.4. Decomposition of molecular diffusion

Recent works [62,63] on turbulent nonpremixed combustion found that molecular diffusion along the direction tangential to Z isosurfaces may play important roles. In this regime, the classical flamelet theory [64], which assumes that the combustion occurs rapidly within a thin layer near Z_{st} and is predominately driven by normal-to-Z diffusion, needs to consider the tangential-to-Z diffusion effects. To investigate the effects of tangential-to-Z diffusion on edge-flame propagation dynamics, as will be shown in Section 3.7, we decompose the displacement speed S_C into components due to diffusion along directions normal ($\perp$) and tangential ($\parallel$) to Z isosurfaces, as schematically illustrated by Fig. 3. Following the coordinate systems introduced in this figure, a diffusion term that obeys the form of a Laplacian operator, e.g., $[\mathbf{D}]_k = \nabla\cdot(\rho D_k\nabla Y_k)$, can be decomposed into the gradient and

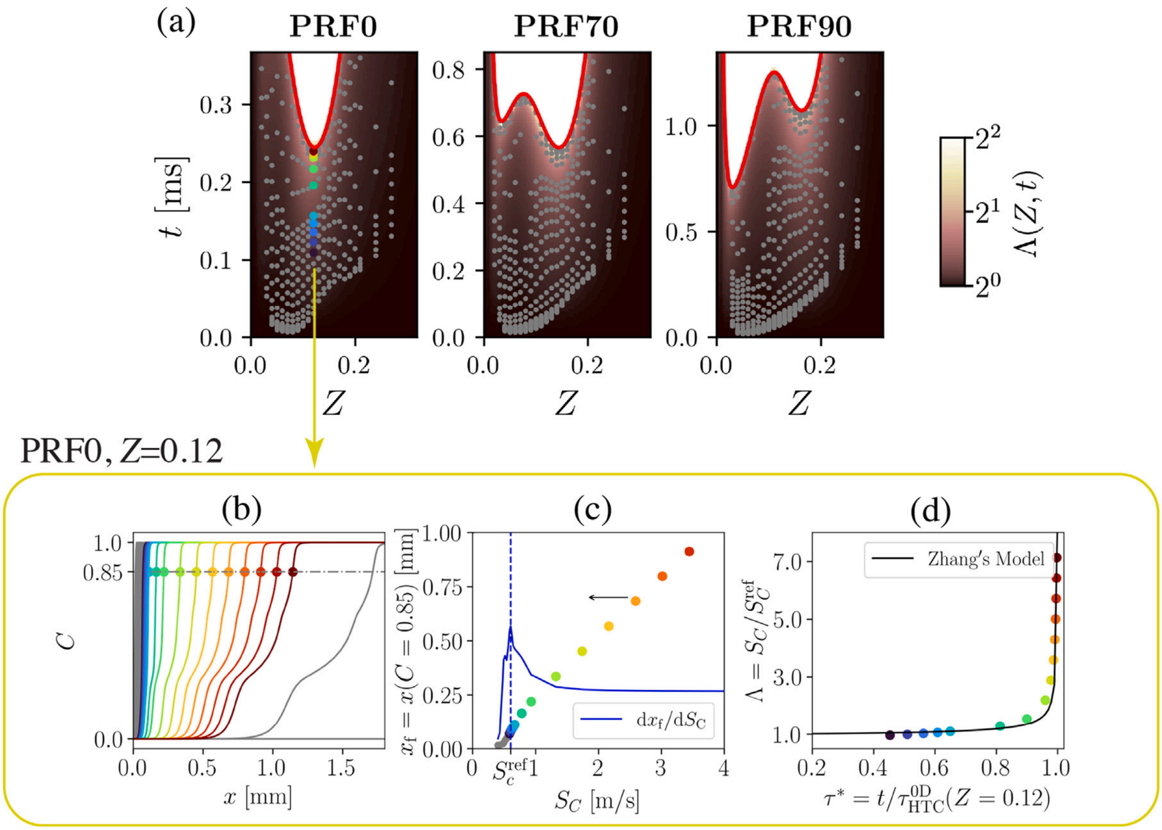

Fig. 2. Effect of autoignition on flame displacement speed based on 1D premixed flame simulations. The upper group (a) shows the contour of acceleration factor $\Lambda = S_C/S_C^{\mathrm{ref}}$ in $Z-t$ space. The grey dots indicate all the 1D flames featured by different reactant residence times; the coloured dots correspond to those in (b)–(d). The red solid line denotes the HTC ignition delay, $\tau^{\mathrm{0D}}_{\mathrm{HTC}}(Z)$. The lower group (b)–(d) shows an example for 1D premixed flames of PRF0, $Z = 0.12$ with increasing (blue to red lines) residence times, including (b) the distribution of C with the flame location x_{f} denoted by dots, (c) the dependence of x_{f} on the local flame displacement speed S_C and (d) the dependence of acceleration factor on the normalised residence time τ^*. The dots in (c) and (d) point to the corresponding values extracted at x_{f} as shown by the dots in (b). The Zhang's model refers to Eqs. (5) and (6). Note that t^* and τ^* can be related by a coefficient $\tau^{\mathrm{0D}}_{\mathrm{HTC}}/\tau_{\mathrm{mr}}$. (For interpretation of the references to colour in this figure legend, the reader is referred to the web version of this article.)

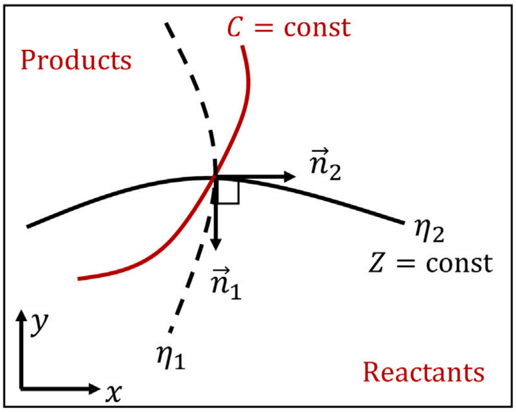

Fig. 3. Local frame rotation for the decomposition of molecular diffusion term in the direction normal and tangential to Z isosurface. The red and black lines denote the C and Z isosurfaces. The x_j and η_i-coordinates refer to the Cartesian and the rotated frame, respectively;. (For interpretation of the references to colour in this figure legend, the reader is referred to the web version of this article.)

divergence operators separately. Specifically, the gradient operator, ∇Y_k, can be decomposed as

$$\nabla Y_k = \nabla_\perp Y_k + \nabla_\parallel Y_k, \tag{7}$$

$$\nabla_\perp Y_k = \vec{n}_1(\vec{n}_1 \cdot \nabla Y_k) = \vec{n}_1 \frac{\partial Y_k}{\partial \eta_1}, \tag{8}$$

$$\nabla_\parallel Y_k = \vec{n}_2(\vec{n}_2 \cdot \nabla Y_k) = \vec{n}_2 \frac{\partial Y_k}{\partial \eta_2}, \tag{9}$$

where

$$\frac{\partial Y}{\partial \eta_1} = \vec{n}_1 \cdot \nabla Y, \tag{10}$$

$$\frac{\partial Y}{\partial \eta_2} = \vec{n}_2 \cdot \nabla Y, \tag{11}$$

are the directional derivatives along $\vec{n}_1$ and $\vec{n}_2$, respectively. The basis vectors $\vec{n}_1$ and $\vec{n}_2$ align with the normal and tangential direction of the Z isosurface, respectively. The divergence operator for vector $\vec{a}$ can be decomposed as

$$\nabla \cdot \vec{a} = \nabla_\perp \cdot \vec{a} + \nabla_\parallel \cdot \vec{a}, \tag{12}$$

$$\nabla_\perp \cdot \vec{a} = \vec{n}_1 \cdot \frac{\partial \vec{a}}{\partial \eta_1}, \tag{13}$$

$$\nabla_\parallel \cdot \vec{a} = \vec{n}_2 \cdot \frac{\partial \vec{a}}{\partial \eta_2}. \tag{14}$$

Therefore, the decomposition of $[\mathbf{D}]_k = \nabla \cdot (\rho D_k \nabla Y_k)$ can be performed by

$$[\mathbf{D}]_k = (\nabla_\perp + \nabla_\parallel) \cdot (\rho D_k \nabla_\perp Y_k + \rho D_k \nabla_\parallel Y_k) \tag{15}$$

$$= \nabla_\perp \cdot (\rho D_k \nabla_\perp Y_k) + \nabla_\parallel \cdot (\rho D_k \nabla_\parallel Y_k) + \nabla_\parallel \cdot (\rho D_k \nabla_\perp Y_k) + \nabla_\perp \cdot (\rho D_k \nabla_\parallel Y_k) \tag{16}$$

$$= \frac{\partial}{\partial \eta_1}\left(\rho D_k \frac{\partial Y_k}{\partial \eta_1}\right) + \frac{\partial}{\partial \eta_2}\left(\rho D_k \frac{\partial Y_k}{\partial \eta_2}\right) + \left(\nabla \cdot \vec{n}_1\right) \rho D_k \frac{\partial Y_k}{\partial \eta_1} + \left(\nabla \cdot \vec{n}_2\right) \rho D_k \frac{\partial Y_k}{\partial \eta_2}. \tag{17}$$

Table 3
Decomposition of $\nabla\cdot(\rho D_k \nabla Y_k)$ along directions normal ($\perp$) and tangential ($\parallel$) to Z isosurfaces.

	Expression	Physical interpretation
$\nabla_\perp \cdot (\rho D_k \nabla_\perp Y_k)$	$\frac{\partial}{\partial \eta_1}\left(\rho D_k \frac{\partial Y_k}{\partial \eta_1}\right)$	Normal diffusion
$\nabla_\parallel \cdot (\rho D_k \nabla_\perp Y_k)$	$-\rho \kappa_Z D_k \frac{\partial Y_k}{\partial \eta_1}$	Normal diffusion associated with κ_Z
$\nabla_\perp \cdot (\rho D_k \nabla_\parallel Y_k)$	$\rho D_k \frac{\partial Y}{\partial \eta_2}(\nabla \cdot \vec{n}_2)$	Tangential diffusion associated with $\nabla \cdot \overrightarrow{n_2}$
$\nabla_\parallel \cdot (\rho D_k \nabla_\parallel Y_k)$	$\frac{\partial}{\partial \eta_2}\left(\rho D_k \frac{\partial Y}{\partial \eta_2}\right)$	Tangential diffusion

The physical interpretation of each component of the diffusion term, $[\mathbf{D}]_k$, can be described as follows. The components equal to $\frac{\partial}{\partial \eta_1}\left(\rho D_k \frac{\partial Y}{\partial \eta_1}\right)$ and $\frac{\partial}{\partial \eta_2}\left(\rho D_k \frac{\partial Y}{\partial \eta_2}\right)$ account for the normal and tangential-to-Z diffusion of the kth species, respectively. The two terms, which are equal to $(\nabla \cdot \vec{n}_1)\rho D_k \frac{\partial Y_k}{\partial \eta_1}$ and $(\nabla \cdot \vec{n}_2)\rho D_k \frac{\partial Y_k}{\partial \eta_2}$, account for the normal- and tangential-to-Z diffusion due to the changing geometry of Z isosurfaces. It is noted that if $\vec{n}_1$ is chosen to be $\vec{n}_1 = -\nabla Z/|\nabla Z|$ then the curvature Z isosurfaces can be expressed as $\kappa_Z = \nabla \cdot \vec{n}_1$ [65] and we have

$$\nabla_\parallel \cdot \left(\rho D_k \nabla_\perp Y_k\right) = \rho D_k \kappa_Z \frac{\partial Y_k}{\partial \eta_1}. \tag{18}$$

The connection between the decomposition of $[\mathbf{D}]_k$ in the ∇ operator form and the equivalent expression including local derivatives, is summarised in Table 3. The term $\nabla \cdot \left[(\rho D_k Y_k/W)\nabla W\right]$ can be decomposed in a similar fashion, such that $S_{C,\mathrm{d}}$ can be expressed as:

$$\begin{aligned}
S_{C,\mathrm{d}} &= \frac{1}{\rho\,|\nabla C|\,\mathcal{Y}_{\mathrm{eq}}}\mathcal{L}_{\mathcal{Y}}\left[\nabla\cdot\left(\rho D_k \nabla Y_k\right) + \nabla\cdot\left(\frac{\rho D_k Y_k}{W}\nabla W\right)\right]\\
&\left.\begin{aligned}
&= \frac{1}{\rho\,|\nabla C|\,\mathcal{Y}_{\mathrm{eq}}}\mathcal{L}_{\mathcal{Y}}\left[\nabla_\perp\cdot\left(\rho D_k \nabla_\perp Y_k\right) + \nabla_\perp\cdot\left(\frac{\rho D_k Y_k}{W}\nabla_\perp W\right)\right]\\
&+ \frac{1}{\rho\,|\nabla C|\,\mathcal{Y}_{\mathrm{eq}}}\mathcal{L}_{\mathcal{Y}}\left[\nabla_\perp\cdot\left(\rho D_k \nabla_\parallel Y_k\right) + \nabla_\perp\cdot\left(\frac{\rho D_k Y_k}{W}\nabla_\parallel W\right)\right]
\end{aligned}\right\} \rightarrow S^{\perp}_{C,\mathrm{d}}\\
&\left.\begin{aligned}
&+ \frac{1}{\rho\,|\nabla C|\,\mathcal{Y}_{\mathrm{eq}}}\mathcal{L}_{\mathcal{Y}}\left[\nabla_\parallel\cdot\left(\rho D_k \nabla_\parallel Y_k\right) + \nabla_\parallel\cdot\left(\frac{\rho D_k Y_k}{W}\nabla_\parallel W\right)\right]\\
&+ \frac{1}{\rho\,|\nabla C|\,\mathcal{Y}_{\mathrm{eq}}}\mathcal{L}_{\mathcal{Y}}\left[\nabla_\parallel\cdot\left(\rho D_k \nabla_\perp Y_k\right) + \nabla_\parallel\cdot\left(\frac{\rho D_k Y_k}{W}\nabla_\perp W\right)\right].
\end{aligned}\right\} \rightarrow S^{\parallel}_{C,\mathrm{d}}
\end{aligned} \tag{19}$$

In the above equation, $S^{\perp}_{C,\mathrm{d}}$ and $S^{\parallel}_{C,\mathrm{d}}$ are the sum of terms with $\partial/\partial\eta_1$ and $\partial/\partial\eta_2$, and are used to denote the contribution of normal- and tangential-to-Z diffusion component of the displacement speed, respectively.

As a brief summary, the displacement speed S_C is decomposed into diffusion $S_{C,\mathrm{d}}$ and chemical reaction $S_{C,\mathrm{r}}$ components, which will be used to analyse the propagation dynamics of LTC and HTC reaction fronts (Section 3.5). The diffusion speed $S_{C,\mathrm{d}}$ is further developed into components including $S^{\perp}_{C,\mathrm{d}}$ and $S^{\parallel}_{C,\mathrm{d}}$, which will be used to identify edge-flame structures (Section 3.7).

3. Results and discussion

The homogeneous ignition behaviour is first discussed in Section 3.1. The 2D instantaneous ignition process and the conditional mean flame structure are presented in Sections 3.2 and 3.3, respectively. This is followed by the formation of ignition kernel (Section 3.4), development of deflagrative flame (Section 3.5), quantitative model for flame displacement speed (Section 3.6) and edge flame dynamics (Section 3.7).

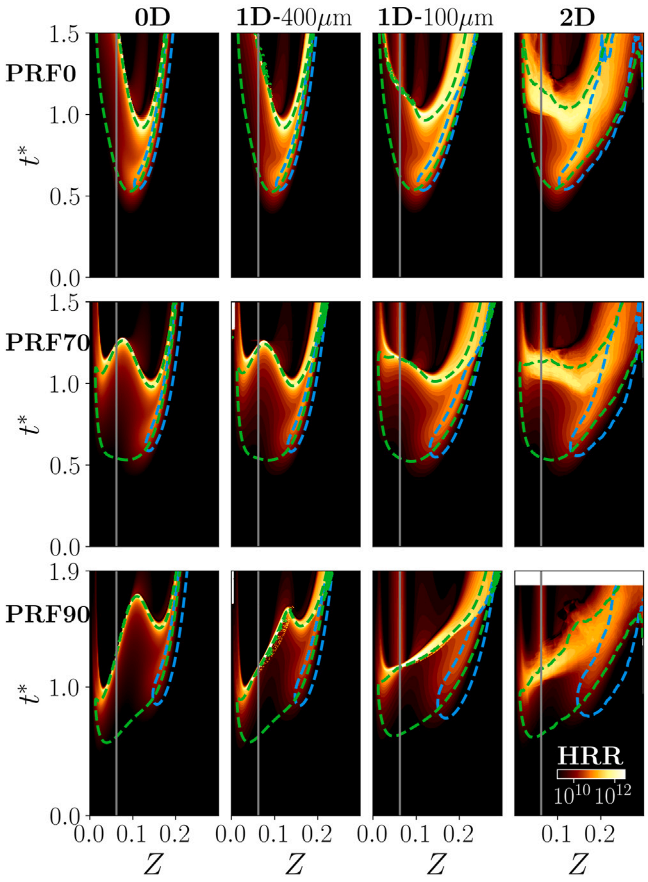

Fig. 4. Temporal evolution of heat release rate (HRR) in Z space. 0D cases denote the transient homogeneous ignition process; 2D cases denote the conditional mean $\langle \mathrm{HRR}|Z\rangle$. Time is normalised by τ_{mr} of each PRF case. The dashed lines denote regions of Y_{KET} ($\langle Y_{\mathrm{KET}}|Z\rangle$ for 2D) $\geq 5\% \times Y^{\mathrm{0D,max}}_{\mathrm{KET}}$ (🟦 🟦 🟦) and $Y_{\mathrm{H2O2}} \geq 5\% \times Y^{\mathrm{0D,max}}_{\mathrm{H2O2}}$ (🟩 🟩 🟩). The vertial grey line denotes the Z_{st}. From top to bottom: PRF0, PRF70 and PRF90. (For interpretation of the references to colour in this figure legend, the reader is referred to the web version of this article.)

3.1. Homogeneous reactor behaviour

For orientation the ignition behaviour in a series of homogeneous (0D) constant pressure reactors is first discussed. We will make reference to the first column of Fig. 4, which shows the HRR contour highlighted by regions with high concentration of H_2O_2 and KET species. Some results from the 1D and 2D DNS cases are also shown in Fig. 4 and will be discussed later.

First, all three PRF mixtures exhibit two-stage ignition in rich mixtures, where a distinct HRR peak due to LTC occurs before the main HTC ignition. The first-stage ignition is preceded by the buildup of Y_{KET} (demarcated by the blue dashed lines), which is then rapidly consumed leading to the first peak of HRR. Subsequently, H_2O_2 is produced (demarcated by the green dashed lines), remains stable during an intermediate stage, and finally breaks down leading to the main stage ignition. As the fraction of i-C_8H_{18} is increased, the two-stage regime is pushed further towards rich mixtures.

Second, addition of i-C_8H_{18} leads to different ignition patterns. For PRF0, a single local minimum of the second-stage ignition delay occurs in rich mixtures. As i-C_8H_{18} is added (PRF70), the ignition delay time is significantly increased (note that the abscissa in Fig. 4 is normalised by τ_{mr} as listed in Table 1). The ignition pattern has qualitatively changed that two local minima of τ_{mr} are observed with comparable ignition delay, though the shorter one still occurs on the fuel rich side. The fuel-lean ignition is closer to Z_{st} and undergoes a single stage, HTC

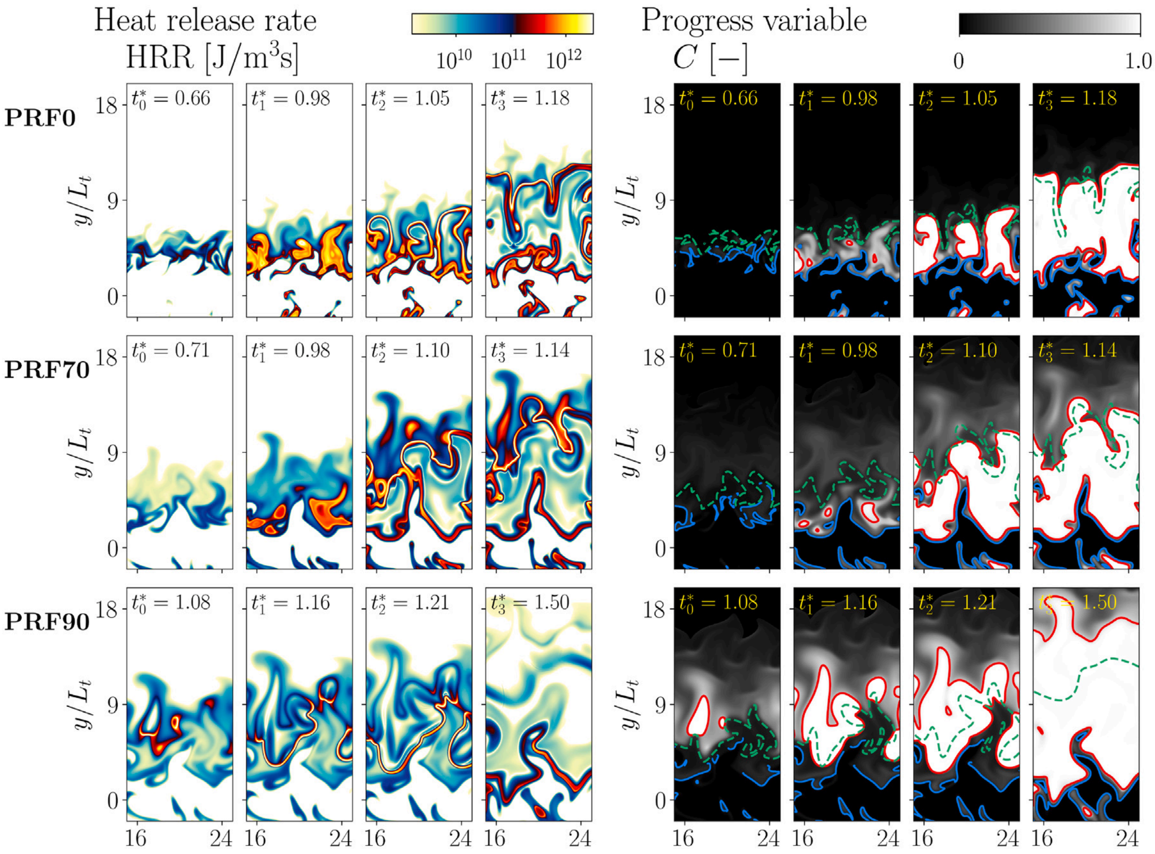

Fig. 5. Contours of heat release rate (HRR) and progress variable (C) within a fixed subdomain for PRF0, 70, 90 case from top to bottom row, at time instants $t_0^* - t_3^*$, normalised by the corresponding τ_{mr} of each PRF case. Dashed lines (- - -) denote Z_{st} isosurfaces in the contour of C. Red and blue solid lines, which corresponds to $C = 0.85$ (——) and $C = 0.1 \cap Z > Z_C$ (——), represent HTC and LTC reaction fronts, respectively. Regions of $y \to 0$ and $y \to \pm 18$ correspond to the fuel-rich and lean side of the mixing layer, respectively. Also note that the nondimensional time instants selected differ slightly between the cases in order to best illustrate the overall behaviour in each case. (For interpretation of the references to colour in this figure legend, the reader is referred to the web version of this article.)

chemistry ignition due to the addition of i-C_8H_{18}. As i-C_8H_{18} continues to increase (PRF90), the fuel-lean ignition is delayed slightly while the fuel-rich ignition is delayed significantly, leading to the first ignition occurring on the fuel-lean side.

As will be shown, these differing behaviours have significant effects on the resulting ignitions in the 2D DNS.

3.2. Qualitative description of ignition transients

An overview of the ignition process for each 2D DNS case is now discussed. Figs. 5 and 6 show the instantaneous heat release rate (HRR), progress variable (C), mass fractions of KET and H_2O_2 species (Y_{KET} and $Y_{H_2O_2}$), and scalar dissipation (χ) contours at different times. These time instants are normalised by the τ_{mr} of each PRF case. A partial field of the whole computation domain is shown to provide a zoom-in view of representative flow features. The stoichiometric (Z_{st}) isosurface is indicated by a dashed line. The HTC and LTC reaction fronts are marked by a red and blue solid line, respectively, in the C contours. In the supplementary material we also provide animations to show the evolution of the entire domain for all three PRF cases.

For PRF0 (pure n-heptane), at $t_0^* = 0.66$, initial HRR is observed on the fuel-rich side. A comparison with the χ and Y_{KET} contours indicates that these initial LTC kernels occur predominantly in regions with low scalar dissipation rate and high values of Y_{KET}. This can be seen from the inset of Y_{KET} and χ at t_0^*. Inspection of $\dot{\omega}_{\mathrm{KET}}$ field (not shown here) indicates that these LTC fronts occur together with local peak of KET consumption rate, suggesting these are locations undergoing first-stage ignition. At around t_1^*, the LTC kernels form into connected, wrinkled reaction fronts. HTC kernels (numerically identified as $C = 0.85$), are observed in fuel-rich mixtures that have been partially reacted by the passing cool flame, accompanied by rapid consumption of H_2O_2. HTC ignition kernels are initiated mostly in regions with relatively low χ. The HTC kernels gradually expand into propagating HTC fronts ($t_1^* - t_3^*$). The HTC fronts moving towards the fuel-rich side gradually catch up with the leading cool flame, burning out the inner mixing layer, while those towards the oxidiser side reach and engulf the Z_{st} surface ($t_3^* = 1.18$).

This overall behaviour in the PRF0 case is broadly consistent with earlier DNS studies in similar configurations especially [27,30,31,34]. One notable difference between the present case and the DME/air cases considered in Refs. [27,34] is that in the present cases the HTC ignition kernels form a connected front and become reasonably well aligned with the Z_{st} isosurface before consuming it, while in [27,34] the stoichiometric isosurface is ignited in multiple discrete locations from which edge flames propagate to consume the contour. This difference is probably attributable to the fact that the HTC reaction fronts in the present case need to travel further until they reach the stoichiometric isosurface. This is a result of two factors: (i) the greater difference in the present case between the most reactive mixture fraction and the stoichiometric mixture fraction (here $Z_{\mathrm{st}} = 0.062$ and $Z_{\mathrm{mr}} = 0.15$, while in Refs. [27,34] $Z_{\mathrm{st}} = 0.1$ and $Z_{\mathrm{mr}} = 0.11$) and (ii) the larger mixing layer thickness ($\delta = 100\,\mu\mathrm{m}$ in the present study vs. $\delta = 25\,\mu\mathrm{m}$ in Refs. [27,34]). The parametric study of n-dodecane flames in Ref. [30] supports this notion, as the importance of edge flames diminished with increased mixing layer thickness, oxygen concentration, and pre-heating, all of which increase the distance between the Z_{st} and Z_{mr} contours.

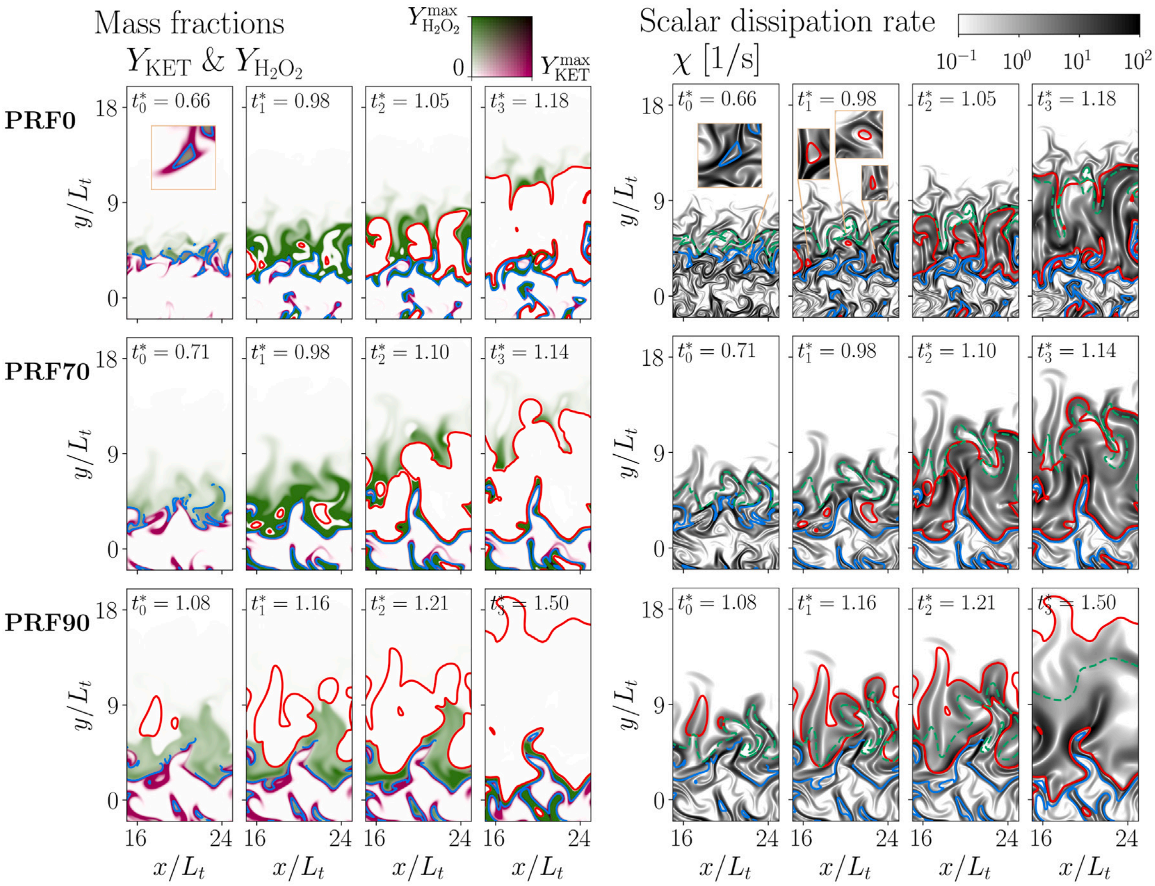

Fig. 6. Contours of mass fractions of KET and H_2O_2 species, and scalar dissipation rate χ in logarithmic scale within a fixed subdomain for PRF0, 70, 90 case from top to bottom row, at time instants $t^*_0 - t^*_3$, normalised by the corresponding τ_{mr} of each PRF case. Dashed lines (- - -) denote Z_{st} isosurfaces in the contour of χ. Red and blue solid lines, which correspond to $C = 0.85$ (━━) and $C = 0.1 \cap Z > Z_C$ (━━), represent HTC and LTC reaction fronts, respectively. Regions of $y \to 0$ and $y \to \pm 18$ correspond to the fuel-rich and lean side of the mixing layer, respectively. Also note that the nondimensional time instants selected differ slightly between the cases in order to best illustrate the overall behaviour in each case. (For interpretation of the references to colour in this figure legend, the reader is referred to the web version of this article.)

For PRF70, the ignition process is similar to PRF0 in that the cool flame kernels commence in fuel-rich regions (around $t^*_0 = 0.71$) and then move quickly as a propagating flame towards rich mixtures. Subsequently, a sequence of HTC kernels emerge (around $t^*_1 = 0.98$) and evolve into HTC fronts in fuel-rich regions. The main difference observed for the PRF70 case compared to the PRF0 case is that significant HRR is observed on the fuel-lean side ($t^*_1 - t^*_2$), which is consistent with the 0D prediction. Isolated HTC kernels appear later in these reacted fuel-lean regions (t^*_2), leading to edge-flame like structures, as exemplified by C contours at t^*_3. A higher level of orthogonality between the HTC reaction front and Z_{st} isoline is observed, though at the beginning the expanding HTC reaction fronts cross Z_{st} isosurface with highly parallel alignment (similar to PRF0). The high level of orthogonality between the HTC reaction front and the Z_{st} isosurface might be a result of two factors. First, initial ignition kernels are formed in both fuel-lean and rich regions, and thus are likely to merge into surfaces that are orthogonal with the Z_{st} isosurfaces. Second, the gradient of ignition delay with respect to Z is low for PRF70 blends, potentially leading to a similar reactivity for the premixtures surrounding Z_{st}. For a reaction front that intersects Z_{st}, its fuel lean and rich premixed wings can propagate at a similar speed compared to the triple point, which also increases the orthogonality level between the leading HTC reaction front and the Z_{st} isosurface. This second argument motivates us to quantitatively examine the propagation speed of HTC fronts, as will be discussed in more details in Section 3.4.

For PRF90, in contrast to the PRF0 and PRF70 cases, HRR kernels first form on the fuel-lean side (around $t^*_1 = 1.08$). Later, these HTC kernels rapidly expand with new fuel-lean kernels emerging ($t^*_2 - t^*_3$). Small isolated rich HRR kernels are observed at very late time ($t^*_4 = 1.5$). This is a difference from the rich-biased HRR kernels in PRF0 and PRF70. It is also found that more edge flames are consuming the Z_{st} isosurface compared to PRF70. These edge flames have essentially a tribrachial structure, including crescent-shaped leading lean and rich branches merging at the triple-point, and a weakly exothermic trailing diffusion branch located on the Z_{st} surface. Differing from [27] there is no upstream LTC branch. By visual inspection of the temporal sequence of the HRR contours, the edge flames are all initiated by the fuel-lean HTC kernels. The appearance of edge flames in this case is suggested to be due to relatively short distance between Z_{mr} and Z_{st}, which is consistent with arguments made above for PRF0. The edge flames terminate due to the collision with other edge flames, or due to merging with the HTC front propagating from lean mixtures and consuming Z_{st} in a more parallel way (as observed in PRF0). The edge flames are trailed by a strong premixed flame propagating towards the fuel-rich region, while the lean branch is gradually weakened due to a lack of fuel.

Overall the behaviour in the 2D cases in terms of the locations where the LTC and HTC ignitions occur and their subsequent progression is qualitatively consistent with expectations from the 0D homogeneous reactors. There are some notable differences, however, which are examined in the following sections.

3.3. Flame structure in mixture fraction-time space

To facilitate a direct comparison of the results from the 2D cases with homogeneous ignitions, and thereby understand the effects of molecular and turbulent mixing on the ignition process, we analyse in this section the temporal evolution of the ignition process and flame evolution in mixture-fraction-time ($Z-t$) space. Here we refer to Fig. 4 again, which shows the results from the 2D DNS, 1D nonpremixed mixing layer and 0D cases.

Going from the 0D case, in which there is no mixing, mixing rates are increased in the $\delta = 400\,\mu\mathrm{m}$ case and further increased in the $\delta = 100\,\mu\mathrm{m}$ case. This results in some important effects. For LTC, as mixing is enhanced, the cool flame progresses faster towards rich mixtures and becomes broader in mixture-fraction space. This is the case for all three PRF blends, and in all cases the cool flame region in the 2D DNS are most similar to the 1D-100 μm case.

For HTC, the enhanced mixing rate also increases the speed at which the HTC fronts progress from the ignition point near Z_{mr} towards relatively leaner and richer mixtures. This can be clearly seen by comparing the 0D cases to the 1D cases for PRF70 and PRF90. In 0D, there are two distinct local minimum of ignition delay, but these are weakened in the 1D-400 μm case and eliminated completely in the 1D−100 μm cases. This is a result of flame propagation from the location of the earliest ignition kernel towards surrounding mixtures. The essential difference between the PRF70 and PRF90 cases is that the ignition occurs on the rich side in the PRF70 case and the flame principally propagates towards lean mixtures to overtake the ignition there while the opposite is true of the PRF90 case. Mixing also results in the appearance of a diffusion flame near Z_{st}, which is enhanced as mixing rate is increased. As turbulent mixing is introduced, the 2D result resemble quite closely the 1D−100 μm in fuel-rich regions but with temporally broadened averaged flame front in Z space. There are more appreciable differences near Z_{st}, which is possibly due to edge flames which propagate along the Z_{st} isosurface rather than parallel to it, as observed in Fig. 5.

The above analysis (Figs. 4 and 5) indicates that the ignition undergoes three main processes, including the formation of ignition kernels, their transition into propagating flames, and consumption of stoichiometric isosurfaces. These processes are examined in detail as follows.

3.4. Initial autoignition kernels

Previous DNS studies of diesel combustion [31,34] indicate that the HTC ignition kernels are mainly initialised in mixtures richer than Z_{mr} and then develop into deflagrative HTC flames. This observation is next investigated for GCI combustion. To allow for a rigorous and consistent identification of the ignition kernels, we define an HTC or LTC kernel by the first appearance of a region fully bounded by $C = 0.85$ or $C = 0.1$ isolines, respectively. Both HTC and LTC ignition kernels emerge in the form of spatially isolated spots. Fig. 7 shows the distribution of 2D initial HTC and LTC ignition kernels in $t-Z$ space, compared to the homogeneous ignition delay times $\tau^{\mathrm{0D}}_{\mathrm{HTC}}(Z)$ and $\tau^{\mathrm{0D}}_{\mathrm{LTC}}(Z)$. The most remarkable observation is that most of the 2D ignition kernels can be well predicted by the local minima in the 0D ignition delay times. Some outliers which ignite earlier than the 0D prediction are observed in fuel-rich regions. This rich-bias behaviour of the initial ignition kernels is qualitatively consistent with previous studies of DME/air (2D, $Da = 0.4$) [34] and n-dodecane/air (3D, $Da = 0.4$) [31] mixing layers, and can be explained by the cool flame progression. Comparing the curve of LTC ignition delay in mixture fraction space of 1D laminar cases (dashed lines in Fig. 7) to that of 0D cases (no diffusion) indicates that the molecular diffusion enhances cool flame propagation. The passage of the cool flame partially reacts the rich mixture and favours the initiation and propagation of HTC combustion as shown by the 1D results. The time interval between initial LTC and HTC ignition kernels decreases as Z increases, as suggested by the 0D and 1D predictions.

It is also found that the departure of the 2D ignition kernels from Z_{mr} is smaller than that observed in Refs. [31,34]. This difference may be explained in terms of cool flame progression. Examination of the flame structure in mixture fraction space (Fig. 4) indicates that increasing molecular and turbulent mixing enhances the propagation of the cool flames, which partially oxidise the mixture and favour the formation of HTC kernels. Comparing the speed of the cool flame progress in Fig. 4 with that in Fig. 6 of Ref. [34] and Fig. 10 of Ref. [31], it is noted that the progression of LTC to rich mixtures is slower in the present work. This is believed to be a result of the weaker turbulent mixing effects in the present cases compared to [34], in which a similar 2D configuration was adopted but with a smaller mixing layer ($\delta = 25\,\mu\mathrm{m}$) and higher initial u' ($= 4.9\,\mathrm{m/s}$), and to [31] in which ignition occurs in 3D shear-driven turbulence, all of which factors lead to strong actions of turbulent mixing.

For PRF70, fuel-lean ignition kernels agree well with the 0D and 1D predictions. For PRF90, the 2D ignition kernels agree well with the 0D case and appear earlier than the 1D ignition. The delayed ignition of 1D case can be explained by the increased χ, which causes radical and heat loss. The turbulent mixing might reduce the mixture-fraction gradient and χ in this region, and thus makes formation of ignition kernels closer to 0D cases compared to 1D cases.

3.5. Transition into deflagrative propagation

The results in Fig. 7 suggest by comparing 0/1/2D cases that the reaction fronts transition from autoignition kernels to diffusively-supported flames. To quantitatively support this observation, a transport budget analysis is conducted for both HTC and LTC reaction fronts. The transport budget analysis is performed by evaluating and comparing the diffusion and reaction terms in Eq. (2) for C. By comparing the relative magnitude of the diffusion and reaction terms, it is possible to distinguish between autoignition and deflagration. Conventionally, a balance of the diffusion and reaction terms has been widely used to demonstrate the presence of a deflagrative flame (e.g., [27]). However, at autoignitive conditions, it should be noted that not much diffusion is needed to sustain a deflagrative flame in a highly reactive environment, as suggested by Dalakoti et al. [38]. In this case, a preheat zone was observed to always exist for deflagration.

Fig. 8 illustrates the trajectory over which the transport budget terms are evaluated. The evaluations are performed by averaging the reaction and diffusion budget terms (that have been normalised by the instantaneous maximum values) along an ensemble of curves as shown by the black lines in Fig. 8. These curves start from the reaction fronts ($C = 0.85$), are locally orthogonal to C isosurfaces and extend towards the direction ahead (+) and behind (−) the flame over a length of 0.8 flame thickness, $\delta_C = 1/|\nabla C|$. Mathematically this procedure can be expressed as

$$\vec{x} = \vec{x}(0) \pm \int_0^{\delta_C} \vec{n}_C(\vec{x})\mathrm{d}s \tag{20}$$

$$C(\vec{x}(0)) = 0.85 \tag{21}$$

where the trajectory $\vec{x} = (x, y)$ is a function of the curve coordinate $\vec{x}(s)$ and is aligned with local normal of C isosurface, $\vec{n}_C$. Eq. (20) is integrated using the forward Euler method with a constant step size of $\Delta s = \Delta x/2$, where Δx is the mesh spacing. This choice ensures that the ensemble used for transport budget evaluation adequately resolves highly curved flame surfaces. Fig. 9 presents the transport analysis for both HTC and LTC reaction fronts. The coordinate s is normalised by the flame thickness δ_C. It is evident that the selected ensemble length of $\pm 0.8 \times \delta_C$ sufficiently covers the reaction zone, as supported by both the instantaneous HRR contours shown in Fig. 8 and the mean C profile in Fig. 9. Furthermore, it is found in Fig. 9 that both LTC and HTC reaction fronts are formed by local autoignition, i.e., reaction dominates over diffusion, and then transition into flames featuring an increasing level of reaction–diffusion balance. As the relative contribution of the diffusion term develops into a relatively steady state (third column of Fig. 9(a) and Fig. 9(b)), a preheat zone, where the diffusion term is larger

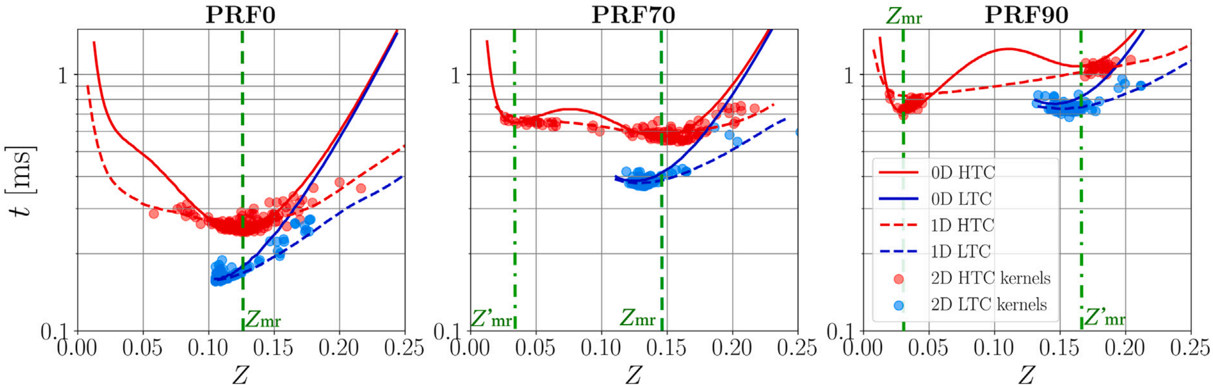

Fig. 7. Comparison of 0D ignition delay times (red/blue solid lines for first/main-stage ignition which are denoted as $\tau^{0\mathrm{D}}_{\mathrm{LTC}}$ and $\tau^{0\mathrm{D}}_{\mathrm{HTC}}$, respectively) with the emergence time of 2D LTC (blue circles) and HTC (red circles) kernels. The propagation of LTC (blue dashed lines) and HTC (red dashed lines) fronts of laminar 1D cases (dashed lines) are shown for reference. The vertical green dashed and dash-dotted lines denote Z_{mr} and Z'_{mr}, respectively. (For interpretation of the references to colour in this figure legend, the reader is referred to the web version of this article.)

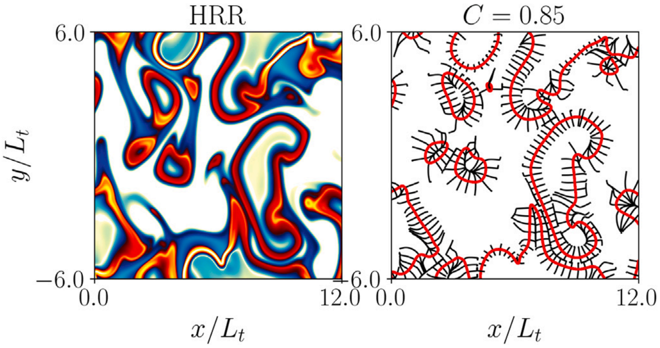

Fig. 8. Illustration for calculating the mean transport budget terms. The HRR contour (left) and the corresponding C = 0.85 isolines in a truncated window are shown for example (PRF70). Transport budget terms are gathered and averaged over an ensemble of curved trajectories (black lines) which start at C = 0.85 and extend along the direction normal to C isolines over a certain length. (For interpretation of the references to colour in this figure legend, the reader is referred to the web version of this article.)

than that of reaction, is observed ahead of the flame. Moreover, the reactants ahead of the diffusively-supported HTC flames are partially reacted, due to either autoignition or the leading LTC flame for the rich side. This can be seen from the C profile (dashed lines in the second and third columns of Fig. 9(b)), which has a value larger than zero at a distance of 0.8 flame thickness ahead of the flame.

Fig. 10 examines the effects of scalar dissipation rate χ on the above transition process for the PRF70 case. The results of PRF0 and PRF90 are qualitatively similar and are provided in the Supplementary Material. The conditional averages are plotted for C, HRR, T, Y_{CH2O}, and Y_{KET} at different instants over the ignition process. The averages are upon Z and three levels of χ, namely low, moderate, and high. The ranges of these three levels of χ are defined by $0 < F_{\chi|Z} < 0.4$, $0.4 < F_{\chi|Z} < 0.8$, and $0.8 < F_{\chi|Z} < 1.0$, where $F_{\chi|Z}$ is the cumulative distribution function of χ conditioned upon Z, i.e., $F_{\chi|Z}(a|\mathrm{Z}) = f(\chi \leq a|Z = \mathrm{Z})$. The conditional means of χ averaged upon each level are also presented in the bottom rows for reference. At the beginning of ignition, and for both LTC and HTC ignitions, increasing χ broadens the local peak of C, T, and HRR profiles while decreasing their local peak values. This indicates that χ inhibits LTC and HTC ignitions by diffusing heat and radicals away from ignition sites to surrounding regions, similarly to what has been previously observed for other fuels [21,31,34,37]. As the ignition develops, the effect of χ is reversed: for both LTC and HTC fronts, χ enhances their transition into deflagrative flames and the subsequent propagation in Z space.

The above analysis indicates the development from autoignition kernels to deflagrative reaction fronts, for both LTC and HTC combustion. This is consistent with the observation made for diesel combustion [31,33,34]. It should be noted that the observed similarity is not obvious considering the significantly different thermochemistry conditions including the location of Z_{mr} to Z_{st}, the distance between Z_{mr} and Z_{st}, and the distribution of ignition delay time in Z space (e.g., the PRF70 case exhibits two comparable local minima of ignition delay instead of one as in all previous works for diesel combustion). When coupled with turbulence these factors will affect local gradients in ignition delay: turbulence can decrease mean gradients (by mixing initially sharp gradients), which favours a spontaneous ignition sequence, or increase local gradients (through straining), which favours a deflagrative sequence.

In the following we focus on the dynamics of HTC reaction fronts due to their dominant contribution to the global HRR.

3.6. Flame displacement speed

For GCI combustion, it is desired to model the flame propagation speed since it can significantly impact the fuel consumption rate and the temporal evolution of in-cylinder HRR and pressure [66]. To that end, we propose a simplified model for predicting the displacement speed S_C for HTC flame and test the model performance against the present DNS dataset.

Previous results, e.g., Figs. 9(b) and 10, indicate that the HTC flame propagates in premixtures with different mixture fraction Z. Moreover, the premixtures are highly autoignitive and thus S_C is expected to be highly dependent on the normalised residence time $\tau^* = t/\tau^{0\mathrm{D}}_{\mathrm{HTC}}(Z)$, which affects the level of how the reactant is partially reacted when the flame passed by. To account for the effects of both varying composition and autoignition, S_C is proposed to be a function of Z and τ^*, and modelled by the following form

$$S_C(Z,\tau^*) = S^{\mathrm{ref}}_C(Z)\Lambda(Z,\tau^*) \tag{22}$$

In Eq. (22), S^{ref}_C is the reference laminar flame speed (or intrinsic deflagration speed) of the premixture with composition Z, and Λ is the acceleration factor. Both of these two parameters are calculated according to the method introduced in Section 2.3. By Eq. (22), we assume that the joint effect of the spatially varying composition and autoignition on flame propagation speed can be decomposed and their respective contribution be written in a product form.

Fig. 11 compares the 2D conditional mean of $\langle S_C|Z\rangle$ (first row) and $\langle S_C/\Lambda|Z\rangle$ (second row) to the 1D referenced flame speeds, $S^{\mathrm{ref}}_C(Z)$. The location Z_{mr} and Z'_{mr} are marked by vertical solid and dashed lines, respectively. The conditional mean is performed on C = 0.85

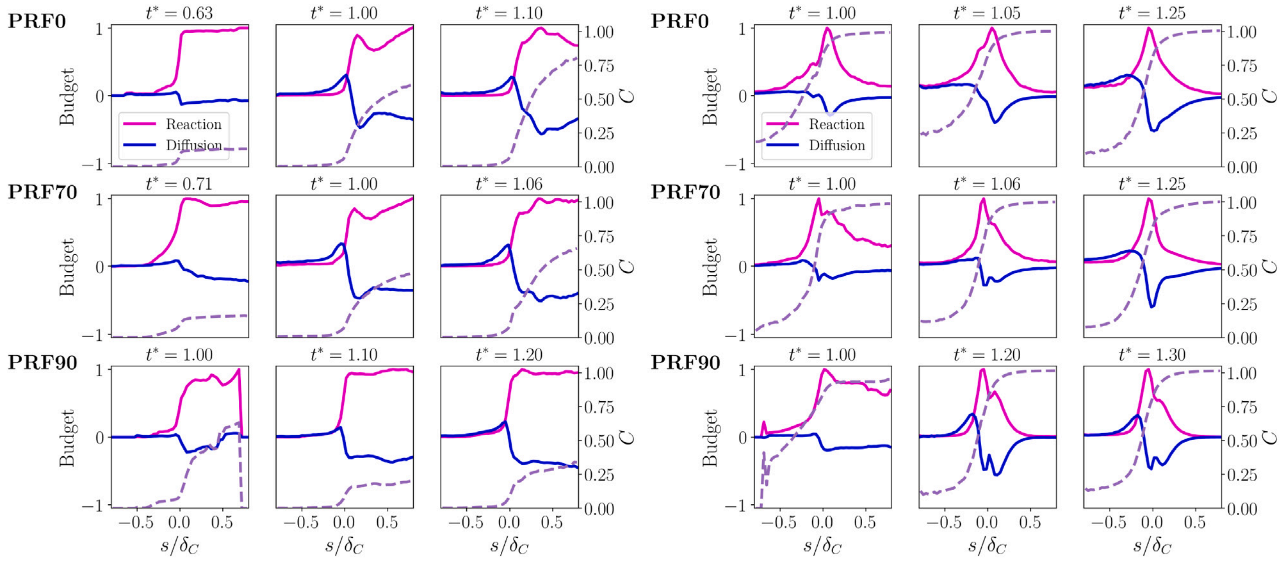

(a) LTC front

(b) HTC front

Fig. 9. Averaged reaction (magenta) and diffusion (blue) budget terms, and progress variable across (a) LTC and (b) HTC reaction fronts at different times. The budget terms have been normalised by the maximum value for each case. (For interpretation of the references to colour in this figure legend, the reader is referred to the web version of this article.)

isosurfaces, and only those with $\tau^* <= 0.99$ are considered since current modelling of Λ requires $\tau^* < 1.0$, i.e., the residence time of the reactant at the flame surface is shorter than 0D the ignition delay. In the present case, the HTC fronts with $\tau^* > 1.0$ are mostly associated with initial ignition kernels and those with $\tau^* <= 0.99$ account for a majority of the total HTC fronts observed. In more complex scenarios, e.g., 3D turbulence with stronger mixing, the ignition would be significantly delayed compared to the 0D cases (e.g., see [67]) and more flames with $\tau^* > 1$ are likely to be encountered. In this case, the actual ignition delay may depend on mixing history and departs significantly from the 0D case.

The trend of $\langle S_C|Z\rangle$ and $\langle S_C^{\mathrm{ref}}|Z\rangle$ are qualitatively similar, both peaking near stoichiometry and decreasing towards zero in either very lean or rich conditions. The magnitude of $\langle S_C|Z\rangle$ is overall higher than the 1D reference case. Moreover, there are high values of $\langle S_C|Z\rangle$ observed near Z_{mr} and Z'_{mr}, due to the initial ignition kernels of which the reaction component of the displacement speed dominates over the diffusion component, as shown by Fig. 9(b). When the effects of autoignition is considered by correcting S_C with Λ, $\langle S_C/\Lambda|Z\rangle$ agrees well with $S_C^{\mathrm{ref}}(Z)$ except for the very rich mixtures of PRF0 and PRF70. Such agreement supports that the displacement speed of HTC fronts depend on both the mixture composition and autoignition, and Eq. (22) is performant in modelling these effects.

To further examine the performance of the S_C model implied by Eq. (22), Fig. 12 plots the conditional means of several variables extracted on $C = 0.85$ isosurfaces, doubly conditioned upon residence time t and Z. These variables can be roughly categorised into three groups, including (i) the original and corrected displacement speeds, S_C and S_C/Λ; (ii) the original and normalised residence times, t and $\tau^* = t/\tau_{\mathrm{HTC}}^{\mathrm{0D}}$ and the interpolated acceleration factor Λ, and (iii) flame curvature $\kappa_C = -\nabla \cdot \vec{n}_Z$, heat release rate (HRR) and the alignment factor $k = \vec{n}_C \cdot \vec{n}_Z$ between the C and Z isosurfaces.

The results show that the enhancement of S_C by autoignition depends on both turbulent mixing and fuel chemistry (which determines $\tau_{\mathrm{HTC}}^{\mathrm{0D}}(Z)$ given a thermochemistry condition). For all three PRF cases, Λ has the highest value of about 3–4 near Z_{mr} or Z'_{mr} where initial ignition kernels occur with τ^* close to 1. The turbulent mixing affects the timing of transition into deflagrative flames and their propagation in Z space, as shown by Fig. 10. As a result the HTC fronts arrive at a given Z with different τ^* and Λ, as can be seen from the profiles of $\langle t|Z\rangle$, $\langle \tau^*|Z\rangle$, and $\langle \Lambda|Z\rangle$. As a result, the flames undergo different levels of enhancement due to autoignition. Also due to the turbulent mixing, the flames progress into the very rich and lean regions much faster than what 0D cases predict. As a result τ^* reduces away from 1 and the enhancement of autoignition is greatly weakened. One interesting parameter is the mixture range $Z \in \Delta Z = \left[\min(Z_{\mathrm{st}}, Z_{\mathrm{mr}}, Z'_{\mathrm{mr}}), \max(Z_{\mathrm{st}}, Z_{\mathrm{mr}}, Z'_{\mathrm{mr}})\right]$, wherein the flame heat release rate (HRR), propagation speed (S_C) and enhancement of autoignition (Λ) are all high. In this region, the development of the strongest flame that exhibits the highest HRR and propagation speed, is significantly affected by autoignition. The PRF70 case, which represents the typical GCI condition, has the widest range of $\Delta Z = |Z'_{\mathrm{mr}} - Z_{\mathrm{mr}}| \approx 0.12$. This is due to its unique distribution of $\tau_{\mathrm{HTC}}^{\mathrm{0D}}(Z)$, which yields a low gradient of $\tau_{\mathrm{HTC}}^{\mathrm{0D}}$ over Z around Z_{st} and thus the residence time of the reactant is likely to be comparable to the ignition delay as the flame passes by. As a contrast, for PRF90 the enhancement of autoignition is confined to $\Delta Z = |Z_{\mathrm{st}} - Z_{\mathrm{mr}}| \approx 0.03$ at the fuel lean side (though for PRF90 Λ is also high around Z'_{mr} at the fuel rich side, the HRR and S_C are very low there and thus the contribution of autoignition to the global ignition is secondary).

For PRF0 and PRF70, it is also noted that $\langle S_C|Z\rangle$ increases in the very rich mixture, e.g., $Z > 0.2$. There are possibly two reasons. First, the high value of $\langle S_C|Z\rangle$ is due to flame merging at the centre of the double mixing layer. The flame around the merging point forms a cusp shape with negative curvatures as supported by $\langle \kappa_C|Z\rangle$ profiles (see animations in the Supplementary Material). Meanwhile the magnitude of the gradient $|\nabla C|$ ahead of the flame decreases and leads to a high S_C. The second possible reason is that the diffusively-supported LTC reaction front progresses into richer Z much faster than $\tau_{\mathrm{LTC}}^{\mathrm{0D}}$. This can be seen from Fig. 4. Since the dwell between $\tau_{\mathrm{LTC}}^{\mathrm{0D}}$ and $\tau_{\mathrm{HTC}}^{\mathrm{0D}}$ decreases at richer Z, the actual HTC ignition delay $\tau_{\mathrm{HTC}}^{\mathrm{actual}}$ is also significantly shortened compared to the 0D prediction $\tau_{\mathrm{HTC}}^{\mathrm{0D}}$. As a result, the actual normalised residence time $t/\tau_{\mathrm{HTC}}^{\mathrm{actual}}$ is higher than $t/\tau_{\mathrm{HTC}}^{\mathrm{0D}}$, leading to a higher Λ as well as larger S_C.

Another interesting observation is that near Z_{st}, the magnitude of alignment factor $|k|$ reaches a lowest level near where HRR is high. This may correspond to the edge-flame like structure observed before and will be in studied in the next section.

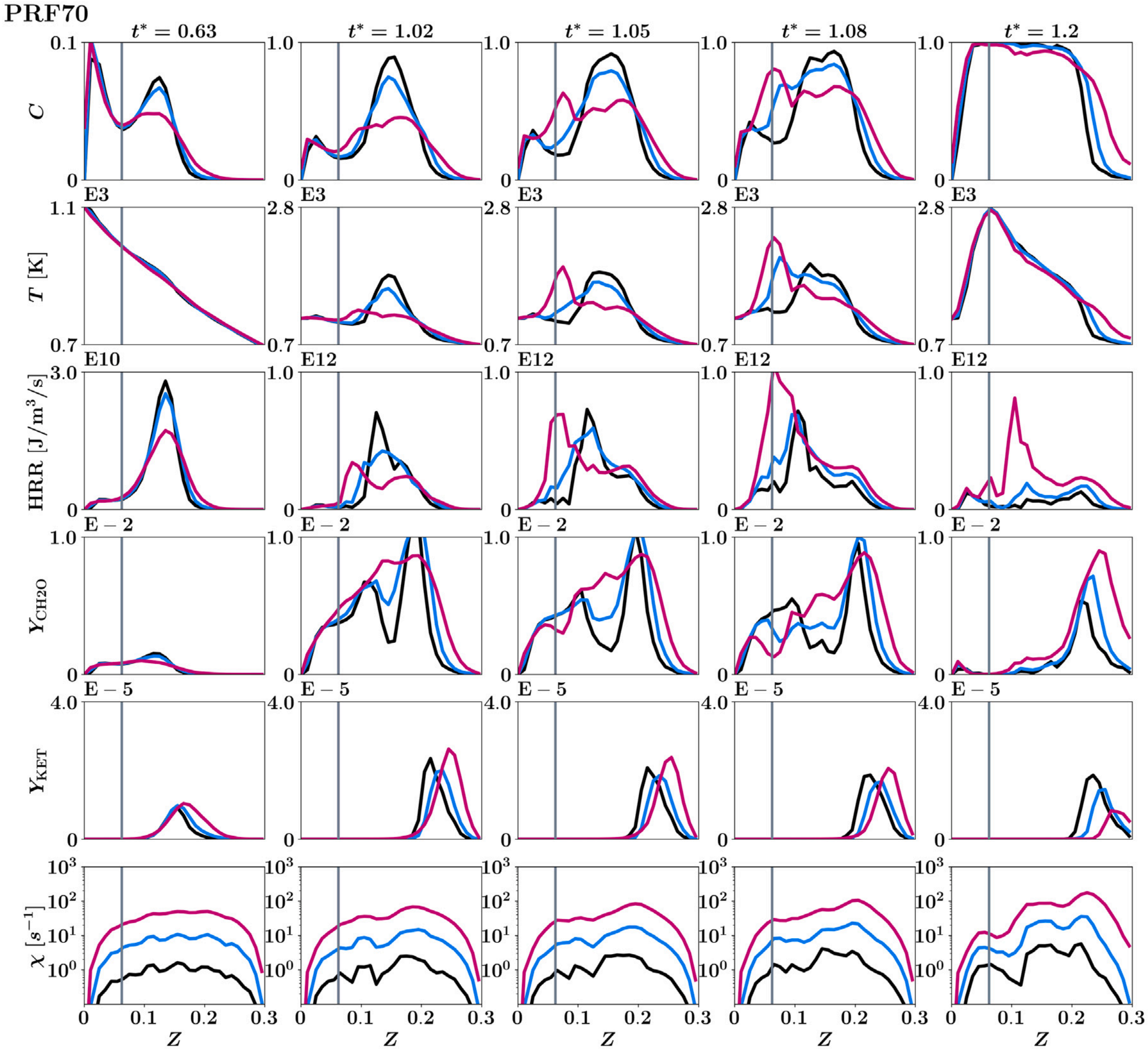

Fig. 10. Conditional averages of progress variable, temperature, heat release rate, mass fractions of formaldehyde and ketohydroperoxides and scalar dissipation rate (from top to bottom rows) of PRF70. The conditioning is upon mixture fraction and scalar dissipation rate at selected instants. Three levels of χ are considered, namely low (black), moderate (blue) and high (purple). The ranges of the different χ levels are defined by $F_{\chi|Z} \in [0, 0.4]$, $[0.4, 0.8]$ and $[0.8, 1.0]$, respectively, where $F_{\chi|Z}$ is the conditional cumulative distribution function of χ, conditioned upon Z. The vertical line denotes Z_{st}. (For interpretation of the references to colour in this figure legend, the reader is referred to the web version of this article.)

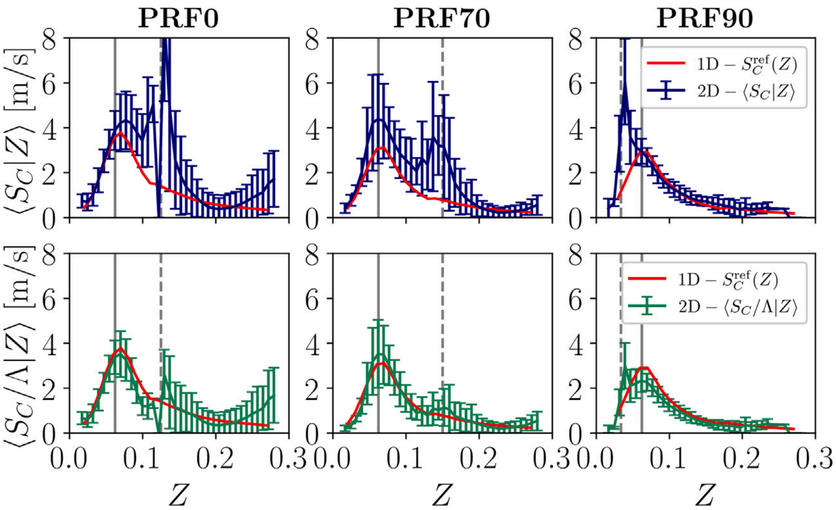

Fig. 11. Comparison of the conditional mean of the original $\langle S_C|Z\rangle$ (first row) and corrected $\langle S_C/\Lambda|Z\rangle$ (second row) displacement speeds, to the 1D referenced laminar premixed flame speeds of different mixture fractions $S_C^{\mathrm{ref}}(Z)$ (red solid line). The error bar indicates the conditional variance. (For interpretation of the references to colour in this figure legend, the reader is referred to the web version of this article.)

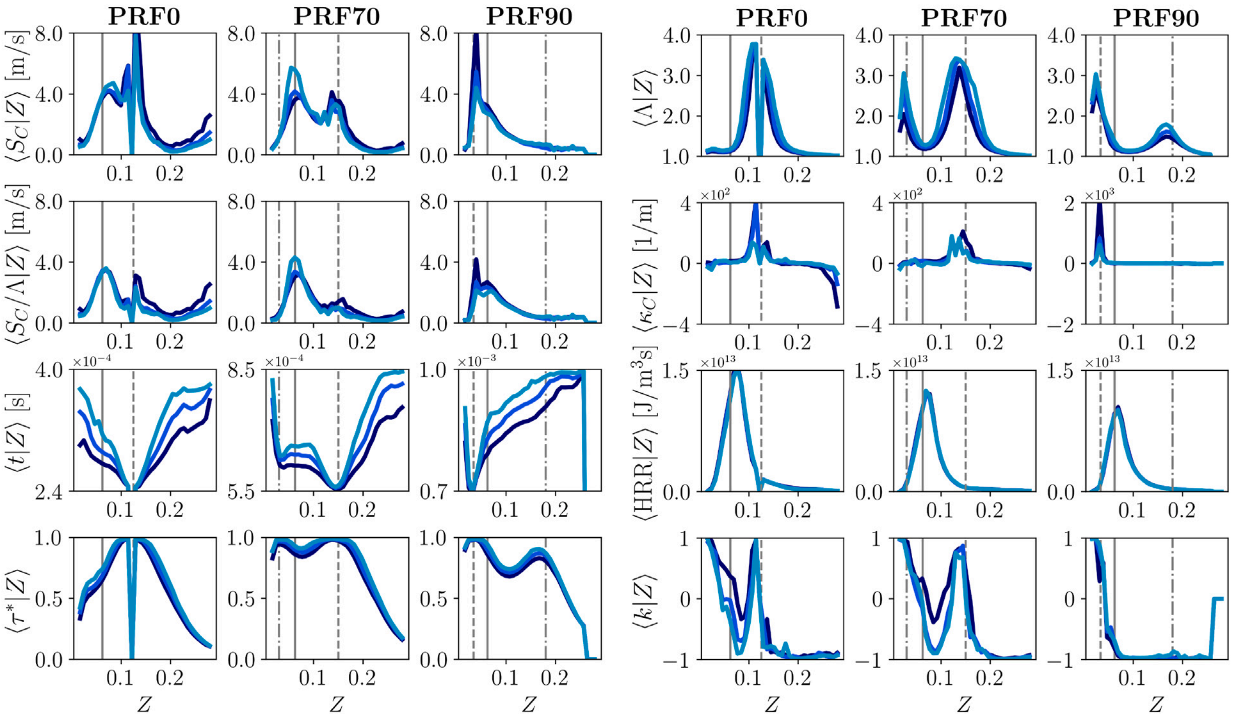

Fig. 12. Conditional averages of variables extracted on HTC fronts ($C = 0.85$), doubly conditioned upon mixture fraction Z and residence time t over all time instants. The left group includes the displacement speed S_C, corrected displacement speed S_C/Λ, residence time t and normalised residence time residence time $\tau = t/\tau_{\mathrm{ig}}(Z)$. The right group includes the acceleration factor Λ, curvature of HTC fronts κ_C, HRR and alignment factor k. Three levels of normalised residence time, τ, are considered, namely low (dark blue), moderate (blue) and high (light blue). The ranges of the different τ levels are defined by $F_{\tau|Z} \in [0.0, 0.4), [0.4, 0.8), [0.8, 1.0)$, respectively, where $F_{\tau|Z}$ is the conditional cumulative distribution function of τ, conditioned upon Z. The vertical solid, dashed and dash-dotted lines denotes Z_{st}, Z_{mr} and Z'_{mr}, respectively. (For interpretation of the references to colour in this figure legend, the reader is referred to the web version of this article.)

3.7. Consumption of Z_{st} isosurface

It was noted earlier that the three PRF cases differ in the mechanism of consumption of the Z_{st} isosurface. This aspect is further examined here.

Following previous works [46], we define an edge flame front as the intersection of the Z_{st} isosurface and HTC ($C = 0.85$) front, as marked by the round dot in Fig. 13. The unburned Z_{st} isosurface is consumed as the edge flame front propagates along Z_{st}. Different propagation modes may exist, such as “edge-flame propagation”, which typically exhibits a tribrachial structure (as observed for PRF70 and PRF90) with the C and Z isosurfaces poorly aligned, or “parallel consumption” with Z_{st} consumed by a HTC front that is mostly parallel to it. These two typical modes are illustrated in Fig. 13. The propagation mode of an edge flame front can be quantitatively characterised by its displacement speed, S_E, which is defined [50] as the flame displacement speed projected into the direction tangential to the Z_{st} isosurface, and is given by $S_e = (S_C - kS_Z)/(1 - k^2)^{1/2}$. Here k is the alignment factor defined as the inner product between the unit vectors normal to the Z and C surfaces, i.e., $k = \vec{n}_Z \cdot \vec{n}_C$; S_C and S_Z denote the displacement speed components contributed by the propagation of C and Z isosurfaces, respectively.

Fig. 13 shows joint PDFs of $k - \chi$ and $S_E - \chi$ gathered at edge flame fronts from all time instants. The conditional means, conditioned upon the scalar dissipation rate χ, are plotted in red dashed lines.

The alignment factor k is first discussed. For PRF0, high alignment ($k \approx 1$) values are observed. These edge flame fronts form as fuel-rich kernels, expand into propagating HTC fronts, and parallelly consume Z_{st}. A few sample points are located near $k \approx -1$; these are due to HTC fronts that traverse Z_{st} and then consume it from the lean side in a direction opposed to $\vec{n}_Z$. For PRF70, a significant number of edge flame fronts exhibit a low level of alignment ($|k| < 0.6$). This is consistent with Fig. 5 which shows that ignition kernels near Z_{st} lead to edge-flame propagation along Z_{st}. Merging of flames originating from rich and lean regions also leads to edge flame fronts with low alignment between $\vec{n}_C$ and $\vec{n}_Z$. For PRF90, k mostly distributes near -1, due to the HTC fronts coming from the lean side. Some marginal samples locate near $k \approx -0.5$, caused by the edge-flame propagation as observed in Fig. 5.

Several features are observed for $S_E - \chi$ correlation. First, the observed S_E is in the order of 1–10 m/s, which is consistent with previous reported edge flame speed near the flame base at diesel conditions [38]. Second, increasing χ leads to higher S_E at regions with high $|k|$ for all three PRF cases. This can be explained by the positive $|k| - \chi$ correlation due to the compressive straining which tends to align scalar gradients, as noted in early studies of passive scalar mixing by [68] and also observed in DNS studies on turbulent premixed [69] and nonpremixed [46] flames. As $|k| \to 1$, the value of S_E is increased via the coefficient $1/\sqrt{1 - k^2}$. The high $|k|$ value indicates the occurrence of parallel consumption, which results from ignition kernels that initiate at some distance to Z_{st}, expand and engulf Z_{st}, or from the scenario wherein unburned and burned Z_{st} isosurfaces are brought together by turbulence, similar the flame folding mechanism in [44]. Third, although edge-flame propagation were observed for PRF70 and PRF90, a negative $S_E - \chi$ correlation that was previously observed in [38,43] is not observed in the present cases. For PRF70, S_E slightly decreases with χ in regions with low alignment ($|k| < 0.5, \chi < 10^1$), suggesting edge-flame propagation. The weak negative dependence of S_E on χ suggests that the edge flames are far from a quenching limit, similar to the findings in [27]. For PRF90, S_E overall increases with χ, indicating that edge-flame propagation is less significant compared to parallel consumption.

For modelling purposes, it is also valuable to differentiate between the parallel consumption and edge-flame propagation modes. This task is challenging based on the statistically averaged results like Fig. 13

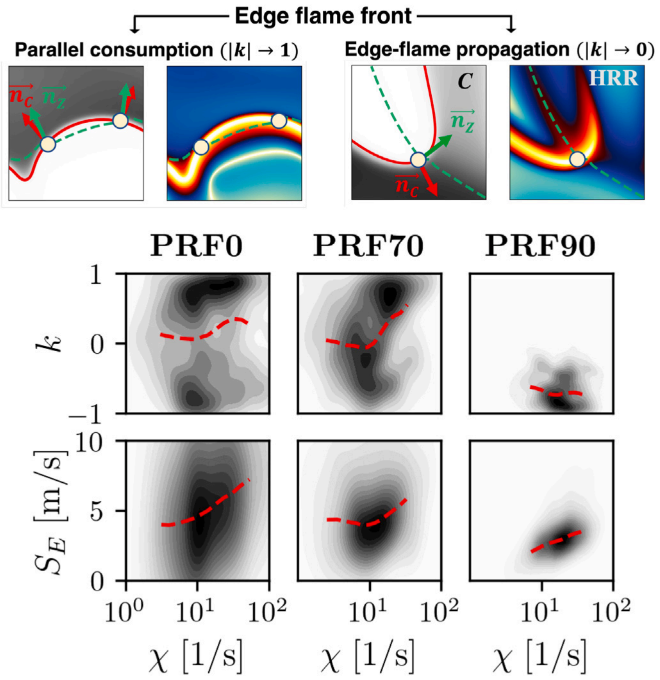

Fig. 13. First row: examples of edge flame front (the corresponding location is marked by a round dot) as the interaction of $C = 0.85$ (red solid) and $Z_{\rm st}$ (green dashed) isosurfaces. The colour scheme of the contour is the same as Fig. 5. Second and third rows: joint PDF of k-χ and S_E-χ for PRF0, 70 and 90 cases (from left to right column). The red dashed line indicates the conditional mean. (For interpretation of the references to colour in this figure legend, the reader is referred to the web version of this article.)

since different modes are mixed together. An alternative is to use the alignment between the flame and $Z_{\rm st}$ isosurface but the identification may depend on the specific choice of threshold value for $|k|$. Here we examine the contribution of different diffusion components to the flame displacement speed. The rational is that, for parallel consumption mode, the normal-to-Z diffusion is expected to prevail over the tangential-to-Z diffusion in the vicinity of $Z_{\rm st}$, similar to the assumption adopted by the conventional nonpremixed flamelet concept [64]. While for the edge-flame mode, the propagation of the edge flame front along $Z_{\rm st}$ should be dominantly driven by the tangential-to-Z diffusion. To examine the relative importance of normal- and tangential-to-Z diffusion, an algorithm is proposed to track each edge flame front separately and the evolution of local diffusion components, $S_{C,\rm d}^{\perp}$ and $S_{C,\rm d}^{\parallel}$ are compared. More specifically, the evolution of each edge flame front is labelled with a unique index and tracked from its inception, i.e., when an HTC reaction front first intersects the $Z_{\rm st}$ isosurface, to its termination when it merges with another edge flame front.

Fig. 14 shows the example of the edge flame fronts that appear within a fixed window in the PRF70 case. As an example of the evolution of the edge flame fronts, consider fronts #18 and #19. By $t^* \approx 1.05$, these two fronts have formed after the HTC reaction front arrives at the $Z_{\rm st}$ isosurface. The portion of the $Z_{\rm st}$ isosurface encompassed by the HTC reaction front is highlighted to demarcate the burned (cyan line) and unburned (black line) regions. As the HTC reaction front expands, the edge flame fronts #18 and #19 propagate into the unburned premixture ($t^* \approx 1.05$–1.07) along the $Z_{\rm st}$ isosurface. The edge flame front #19 terminates after merging with #39 ($t^* \approx 1.09$), and #18 terminates after merging with #57 ($t^* \approx 1.11$). Other interesting edge flame fronts include #70 and #73, which form close to $Z_{\rm st}$ and exhibit features of edge-flame mode. The samples of edge flame fronts shown here are representative of the entire domain.

Figs. 15 and 16 illustrate the changes of $S_{C,\rm d}^{\parallel}$ and $S_{C,\rm d}^{\perp}$ as an edge flame front transitions between the parallel consumption and edge-flame propagation modes. Three examples, namely PRF0-#2, PRF70-#3 and PRF90-#38 are chosen from the three PRF cases to demonstrate the generality. Fig. 15 shows the local fields of HRR and C that surround the selected edge flame fronts. The view range is temporally adjusted to locate the edge flame front at the centre of the image. Six time instants ($t_i^{e,*}$) are chosen to be evenly distributed over the period starting from the formation ($t_0^{e,*}$) to the termination ($t_5^{e,*}$) of each edge flame front. Thus the values of $t_i^{e,*}$ differ for each flame. Fig. 16 plots the temporal evolution of $S_{C,\rm d}^{\parallel}$, $S_{C,\rm d}^{\perp}$ and the alignment factor k extracted at each edge flame front shown in Fig. 15. The time instants in Figs. 15 and 16 correspond and the two figures are discussed together.

The edge flame fronts PRF0-#2 and PRF70-#3 form as an HTC reaction front intersects a $Z_{\rm st}$ isosurface. At $t_0^{e,*}$, the HTC reaction front and $Z_{\rm st}$ isosurface are highly aligned ($k \rightarrow 1$), as shown by the normal vectors of isosurfaces in C contours as well as the alignment factor k. The magnitude of normal diffusion $|S_{C,\rm d}^{\perp}|$ is larger than the tangential component $|S_{C,\rm d}^{\perp}|$. During $t_0^{e,*}$–$t_1^{e,*}$, both PRF0–#2 and PRF70–#3 develop into a tribrachial edge-flame structure, with two premixed branches and a diffusion branch merging at the leading triple point. Meanwhile, $|S_{C,\rm d}^{\parallel}|$ gradually increases and becomes larger than $|S_{C,\rm d}^{\perp}|$ after $t_1^{e,*}$. The two edge flame fronts continue to propagate along $Z_{\rm st}$ during $t_1^{e,*}$–$t_5^{e,*}$ and $|S_{C,\rm d}^{\parallel}|$ keeps larger than $|S_{C,\rm d}^{\perp}|$. Both PRF0–#2 and PRF70–#3 merge with another front originating from the opposite direction after $t_5^{e,*}$. The PRF90-#38 edge flame front shows similar progress compared to PRF0-#2 and PRF70-#3. It forms as an HTC front arrives at $Z_{\rm st}$ from the fuel-lean side with the two isosurfaces highly aligned ($t_0^{e,*}$) and then develops into a tribrachial edge-flame structure ($t_1^{e,*}$–$t_2^{e,*}$). At around $t_3^{e,*}$, the PRF90-#38 enters a region where the $Z_{\rm st}$ isosurface is wrinkled into a corner shape, and one of the premixed branches merges with the diffusion branch. Meanwhile k increases and the magnitude of normal diffusion component $|S_{C,\rm d}^{\perp}|$ is larger than the normal $|S_{C,\rm d}^{\parallel}|$, featuring the parallel consumption mode. After $t_4^{e,*}$ the edge flame front recovers to a triple branch structure with $|S_{C,\rm d}^{\parallel}| > |S_{C,\rm d}^{\perp}|$. Based on these observations, the edge-flame propagation mode is numerically identified as $|S_{C,\rm d}^{\parallel}| > |S_{C,\rm d}^{\perp}|$ and is marked by the grey colour in Fig. 16. As expected, $|S_{C,\rm d}^{\perp}|$ and $|S_{C,\rm d}^{\parallel}|$ are positively and negatively correlated with $|k|$, respectively.

4. Conclusion

With a view to improving understanding of ignitions in GCI engines, DNS of the igniting double mixing layers subject to 2D turbulence were considered. Three cases with PRF0, PRF70 and PRF90 were reported. The analysis focussed on structural comparisons in physical space and mixture-fraction space, the propagation dynamics and displacement speed, supported by statistics of edge flame fronts to understand the mode of consumption of the stoichiometric isocontours. In the following we list the main findings.

- All three PRF blends exhibited two-stage ignition in rich mixtures over a range of mixture fractions. In all cases cool flames were observed that propagated via diffusive support towards the rich side at a rate that exceeded expectations from homogeneous ignition delays. The present study therefore provides further evidence that diffusively supported propagating cool flames are a general feature of nonpremixed ignitions in the 2-stage ignition regime.
- HTC ignition proceeded first in rich mixtures for PRF0, and first in lean mixtures for PRF90. PRF70 exhibited an intermediate behaviour with distinct HTC ignition kernels occurring in both rich and lean mixtures, with the rich ignitions being dominant. These behaviours agreed well with the prediction by homogeneous reactors. The process of HTC progression from ignition kernels towards surrounding mixtures was also demonstrated to

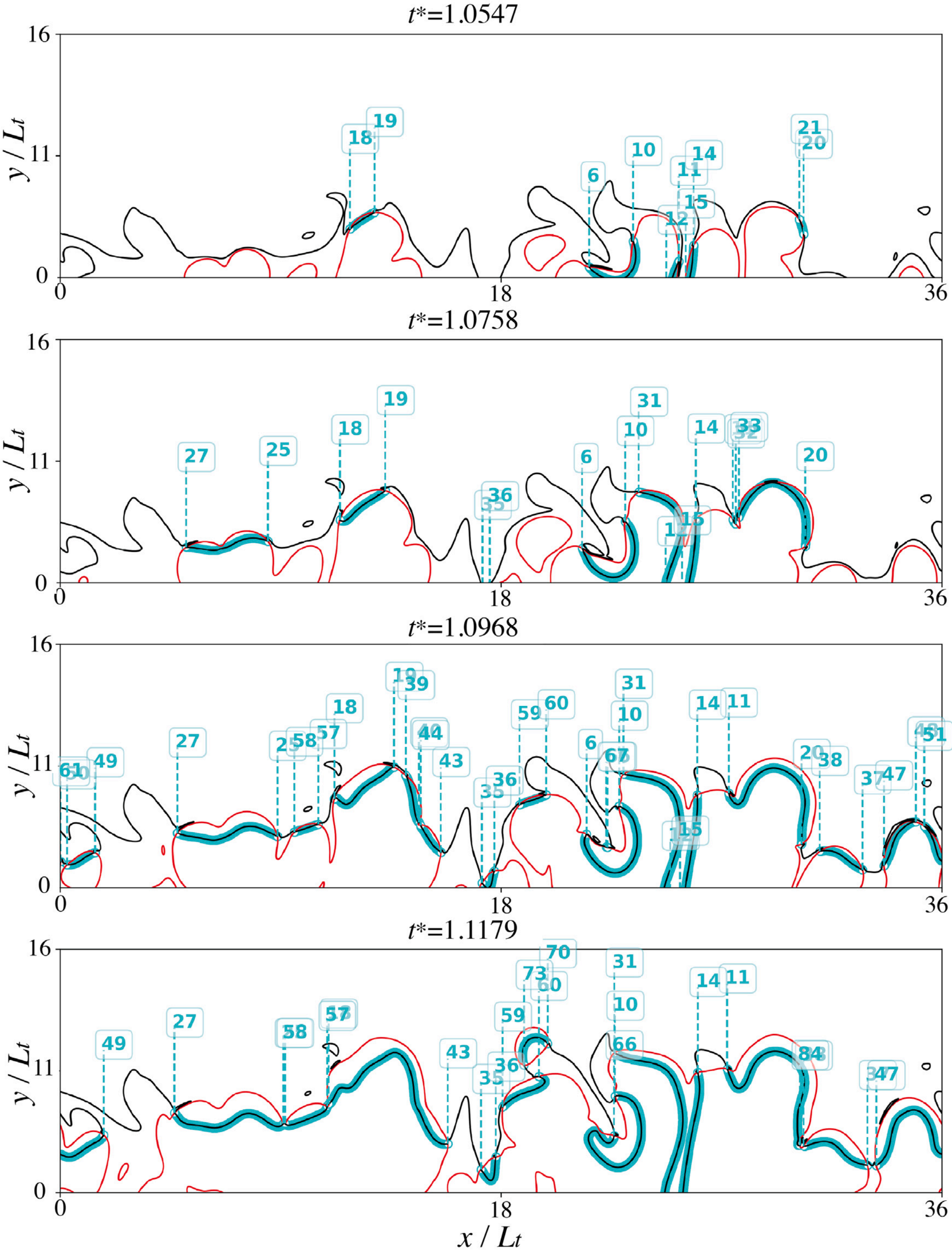

Fig. 14. Example of the edge flame fronts extracted from the PRF70 case. The intersections of HTC reaction fronts ($C = 0.85$, —) and Z_{st} isosurfaces (—) correspond to the locations of edge flame fronts, each of which is tracked by labelling with an unique index as shown in the text boxes. Line segments of Z_{st} isosurfaces within any enclosed HTC isostructures are highlighted (—) to mark the ignited portion. (For interpretation of the references to colour in this figure legend, the reader is referred to the web version of this article.)

be diffusively supported in all three PRF cases as demonstrated by the diffusion-reaction transport budget analysis. The scalar dissipation rate is found to inhibit the formation of ignition kernels while enhancing their transition into deflagration and subsequent propagation in mixture fraction space.

- The displacement speed of the HTC front is highly dependent on the (a) the intrinsic 1D deflagrative flame speed of the local composition in the mixing layer, and (b) the residence time of the premixture that the HTC flame passed by. The autoignition enhances flame propagation by partially reacting the premixture, particularly when the residence time of the reactant is comparable to its ignition delay time. Such effect can be quantitatively measured by a proposed acceleration factor, which can be obtained from the ratio of 1D flame speeds with various residence times,

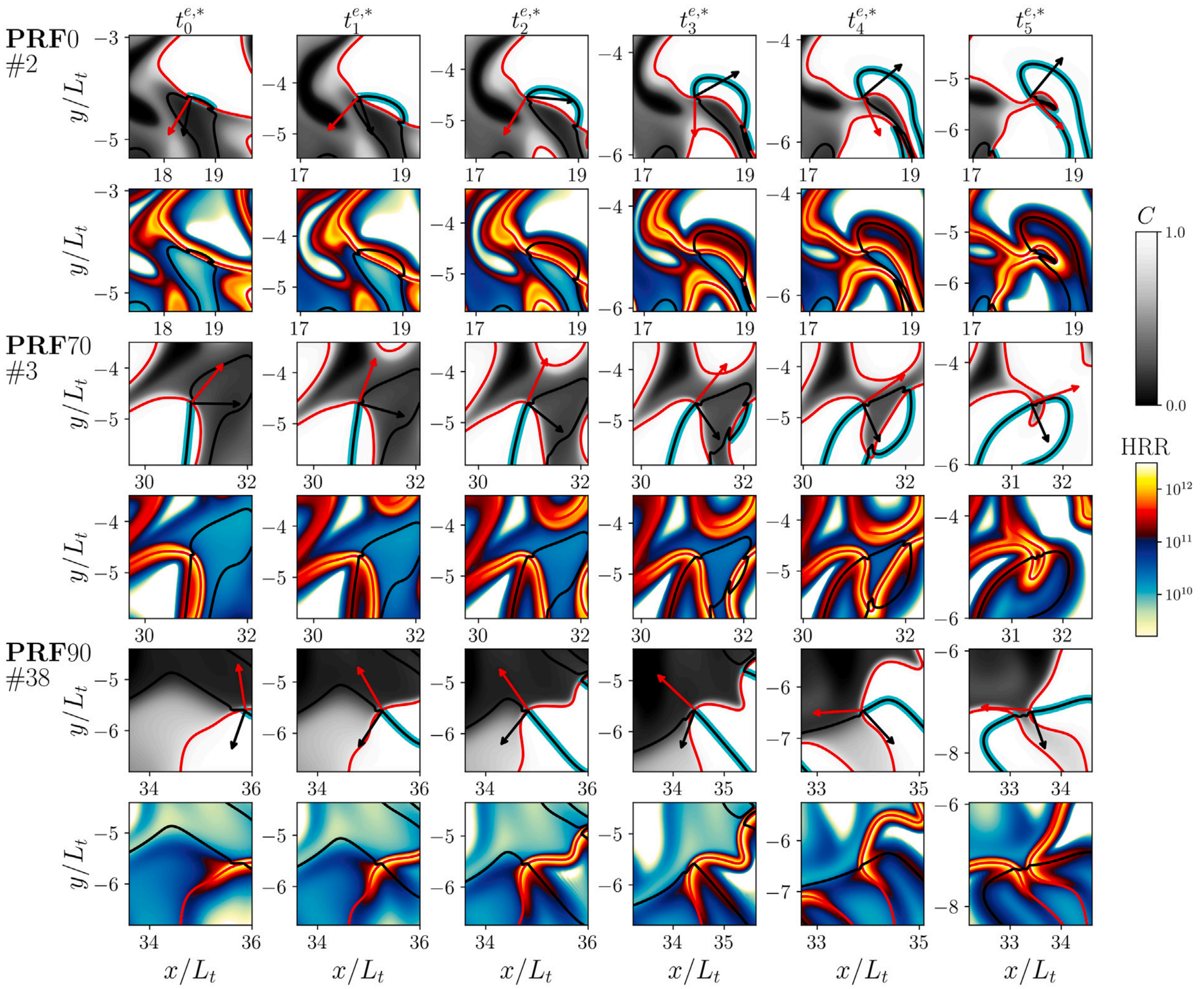

Fig. 15. Example of three edge flame front trajectories, namely PRF0 – #2, PRF70 – #3 and PRF90 – #38 that undergo mixed parallel consumption and edge-flame propagation modes. The contours of C and HRR (upper and lower row of each case, respectively) show the local flame structure at different time instants $t_0^{e,*} - t_5^{e,*}$, which correspond to those shown in Fig. 16. The red and black solid lines denote the HTC and Z_{st} isosurfaces, respectively; the arrows denote the normal direction of $C = 0.85$ and $Z = Z_{\mathrm{st}}$ isosurfaces, respectively. The burned portion of $Z = Z_{\mathrm{st}}$ is marked by cyan colour. (For interpretation of the references to colour in this figure legend, the reader is referred to the web version of this article.)

to the intrinsic deflagrative flame speed. Once corrected by the acceleration factor, the conditional mean displacement speed of the 2D turbulent flame, conditioned upon mixture fraction, agrees well with the reference 1D flame speed. This displacement speed peaks near stoichiometry which leads to a low level of alignment between the HTC flame and the stoichiometric isosurface.

- The mechanism of consumption of the stoichiometric surface was examined considering displacement speed statistics. Two main ignition modes of Z_{st} isosurfaces are found, namely (1) a parallel consumption mode, which occurs as the expanding HTC reaction fronts parallelly consume Z_{st} isosurfaces, wherein normal-to-Z diffusion plays a dominant role, and (2) an edge-flame mode, wherein the edge flame front is curved and exhibits a tribrachial or multibrachial (due to autoignition) structure, wherein the tangential-to-Z diffusion prevails over the normal-to-Z diffusion. For all three PRF cases the statistical results show the stoichiometric surface was consumed mainly by the parallel consumption mode. For PRF70 and 90, discrete ignition kernels near stoichiometry lead to edge-flame propagation, which played a secondary role in consuming the stoichiometric surface.

Overall the results further point to the significant complexity of ignition dynamics in compression ignition engines, and demonstrate that it is necessary to consider fuel chemistry in conjunction with turbulent mixing in order to understand even qualitatively how an ignition is likely to proceed. For practical GCI engine design, the result also indicates the importance of autoignition and as a result, the distribution of residence time should be considered as an important design parameter due to its significant influence on the flame displacement speed. The idealised 0D reactor simulations and 1D steady-state flame solutions can be used to estimate the dominant propagation dynamics, e.g., diffusively-supported, autoigniton-assisted or sequential autoignition, by comparing the residence time of the reactant at the flame surface and the corresponding ignition delay time.

Future research could consider the following lines. First, for the current 2D configuration, the effects of mixing layer thickness could be evaluated. Second, a 3D jet case with spatially varying residence time, in contrast to the uniform residence time in the present case, could be carried out, which would allow to study the effects of residence and ignition delay time gradients, as well as mixing history on the flame propagation speed.

CRediT authorship contribution statement

Zisen Li: Writing – original draft, Visualization, Methodology, Investigation. **Evatt R. Hawkes:** Writing – review & editing, Funding

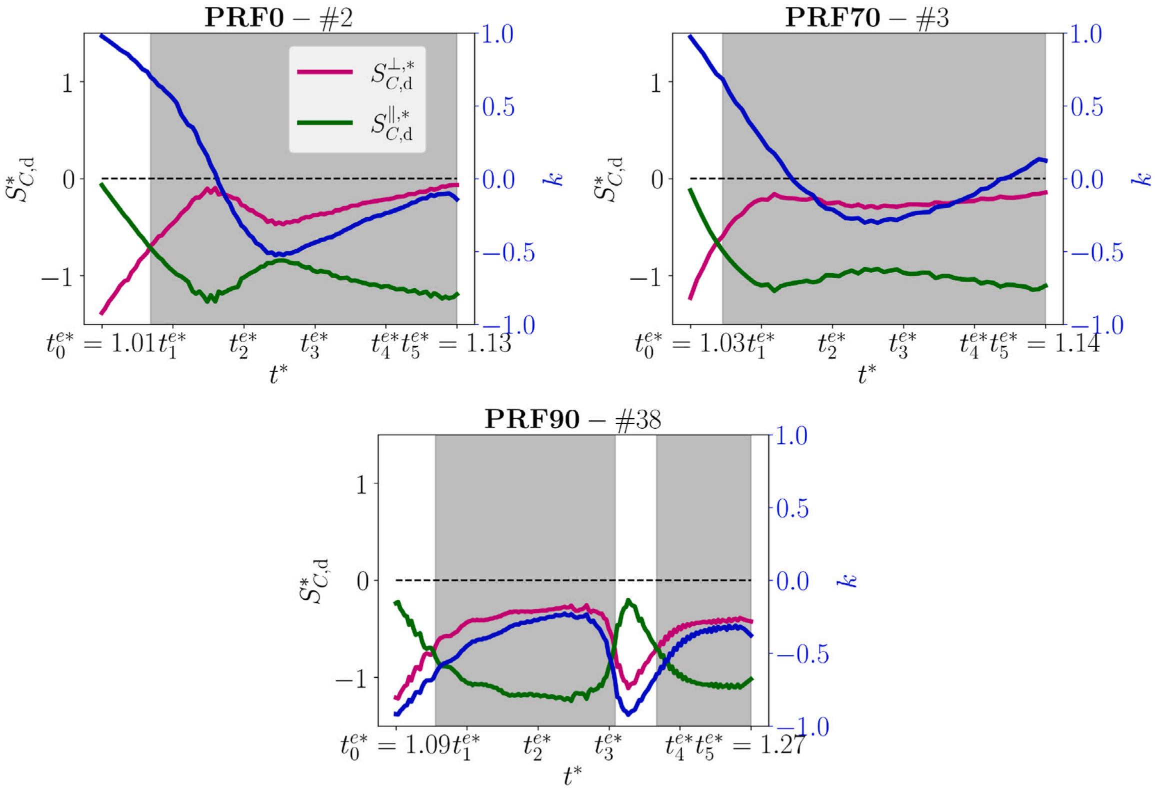

Fig. 16. Temporal evolution of tangential ($S^{\parallel}_{C,\mathrm{d}}$) and normal ($S^{\perp}_{C,\mathrm{d}}$)-to-$Z$ diffusion component of the displacement speed at the three edge flame fronts shown in Fig. 15. The alignment factor, $k = \vec{n}_C \cdot \vec{n}_Z$, is plotted in a secondary axis (coloured by blue). Regions with $|S^{\parallel}_{C,\mathrm{d}}| > |S^{\perp}_{C,\mathrm{d}}|$ are identified as edge-flame mode and shaded by grey colour. (For interpretation of the references to colour in this figure legend, the reader is referred to the web version of this article.)

acquisition, Conceptualization. **Armin Wehrfritz:** Writing – review & editing, Supervision, Investigation. **Bruno Savard:** Writing – review & editing, Supervision, Investigation.

Declaration of competing interest

The authors declare that they have no known competing financial interests or personal relationships that could have appeared to influence the work reported in this paper.

Acknowledgments

This work was supported by the Australian Research Council (ARC, DP180103923). Computational resources were provided by the Australian Government through the Pawsey Supercomputing Centre and the National Computational Infrastructure under the National Computational Merit Allocation Scheme, and by the University of New South Wales.

Appendix A. Supplementary data

Supplementary material related to this article can be found online at https://doi.org/10.1016/j.combustflame.2025.114393.

References

[1] European Commission, EU-vi emission regulation, 2009, Regulation (EC), No. 595/2009.
[2] G.T. Kalghatgi, P. Risberg, H.E. Angstrom, Partially premixed auto-ignition of gaosline to attain low smoke and low NOx at high laod in a compression ignition engine and comparison with a diesel fuel, SAE Tech. Pap. (2007) 2007–01–0006.
[3] M. Sellnau, W. Moore, J. Sinnamon, K. Hoyer, M. Foster, H. Husted, GDCI multi-cylinder engine for high fuel efficiency and low emissions, SAE Int. J. Engines 8 (2) (2015) 775–790.
[4] G. Kalghatgi, B. Johansson, Gasoline compression ignition approach to efficient, clean and affordable future engines, Int. J. Automot. Eng. 232 (1) (2018) 118–138.
[5] G. Kalghatgi, Is it really the end of internal combustion engines and petroleum in transport? Appl. Energy 225 (2018) 965–974.
[6] G.T. Kalghatgi, L. Hildingsson, A.J. Harrison, B. Johansson, Surrogate fuels for premixed combustion in compression ignition engines:, Int. J. Engine Res. (2017).
[7] L. Hildingsson, G. Kalghatgi, N. Tait, B. Johansson, A. Harrison, Fuel octane effects in the partially premixed combustion regime in compression ignition engines, SAE Tech. Pap. (2009) 2009–01–2648.
[8] V. Manente, B. Johansson, P. Tunestal, Partially premixed combustion at high load using gasoline and ethanol–a comparison with diesel, SAE Tech. Pap. (2009) 2009–01–0944.
[9] V. Manente, B. Johansson, W. Cannella, Gasoline partially premixed combustion, the future of internal combustion engines? Int. J. Engine Res. 11 (2011).
[10] M. Sellnau, M. Foster, K. Hoyer, W. Moore, J. Sinnamon, H. Husted, Development of a gasoline direct injection compression ignition (GDCI) engine, SAE Int. J. Engines 7 (2) (2014) 835–851.
[11] Mazda Motor Corporation, Skyaktiv-G: A new-generation highly efficient direct injection gasoline engine that achieves the world's highest gasoline engine compression ratio of 14:1, 2017, URL https://www.mazda.com/en/innovation/technology/skyactiv/skyactiv-g. (Accessed 2021).
[12] M. Lundgren, A. Matamis, Z. Wang, P. Garcia V., M. Richter, O. Andersson, A. Andersson, Lift-off lengths in an optical heavy-duty engine operated at high load with low and high octane number fuels, SAE Tech. Pap. (2018) 2018–01–0245.
[13] C.K. Westbrook, J. Warnatz, W.J. Pitz, A detailed chemical kinetic reaction mechanism for the oxidation of iso-octane and *n*-heptane over an extended temperature range and its application to analysis of engine knock, Symp. (Int.) Combust. 22 (1) (1989) 893–901.
[14] K.S. Jung, S.O. Kim, S.H. Chung, C.S. Yoo, On the flame structure and stabilization characteristics of autoignited laminar lifted *n*-heptane jet flames in heated coflow air, Combust. Flame 223 (2021) 307–319.
[15] C.A. Idicheria, L.M. Pickett, Formaldehyde visualization near lift-off location in a diesel jet, SAE Trans. 115 (2006) 683–695.
[16] J.E. Dec, Advanced compression-ignition engines-understanding the in-cylinder processes, Proc. Combust. Inst. 32 (2) (2009) 2727–2742.
[17] M.P.B. Musculus, P.C. Miles, L.M. Pickett, Conceptual models for partially premixed low-temperature diesel combustion, Prog. Energy Combust. Sci. 39 (2) (2013) 246–283.

[18] Y. Pei, E.R. Hawkes, M. Bolla, S. Kook, G.M. Goldin, Y. Yang, S.B. Pope, S. Som, Modelling *n*-dodecane spray and combustion with the transported probability density function method, Combust. Flame 168 (2016) 420–435.

[19] A. Wehrfritz, O. Kaario, V. Vuorinen, B. Somers, Large eddy simulation of *n*-dodecane spray flames using Flamelet Generated Manifolds, Combust. Flame 167 (2016) 113–131.

[20] E. Mastorakos, Ignition of turbulent non-premixed flames, Prog. Energy Combust. Sci. 35 (1) (2009) 57–97.

[21] E. Mastorakos, T.A. Baritaud, T.J. Poinsot, Numerical simulations of autoignition in turbulent mixing flows, Combust. Flame 109 (1) (1997) 198–223.

[22] S. Sreedhara, K.N. Lakshmisha, Direct numerical simulation of autoignition in a non-premixed, turbulent medium, Proc. Combust. Inst. 28 (1) (2000) 25–33.

[23] S. Sreedhara, K.N. Lakshmisha, Autoignition in a non-premixed medium: DNS studies on the effects of three-dimensional turbulence, Proc. Combust. Inst. 29 (2) (2002) 46–49.

[24] T. Echekki, J.H. Chen, Direct numerical simulation of autoignition in non-homogeneous hydrogen-air mixtures, Combust. Flame 134 (3) (2003) 169–191.

[25] C.S. Yoo, R. Sankaran, J.H. Chen, Three-dimensional direct numerical simulation of a turbulent lifted hydrogen jet flame in heated coflow: flame stabilization and structure, J. Fluid Mech. 640 (2009) 453–481.

[26] R. Yu, X.S. Bai, Direct numerical simulation of lean hydrogen/air auto-ignition in a constant volume enclosure, Combust. Flame 160 (9) (2013) 1706–1716.

[27] A. Krisman, E.R. Hawkes, M. Talei, A. Bhagatwala, J.H. Chen, Characterisation of two-stage ignition in diesel engine-relevant thermochemical conditions using direct numerical simulation, Combust. Flame 172 (2016) 326–341.

[28] Y. Minamoto, J.H. Chen, DNS of a turbulent lifted DME jet flame, Combust. Flame 169 (2016) 38–50.

[29] G. Bansal, A. Mascarenhas, J.H. Chen, Direct numerical simulations of autoignition in stratified dimethyl-ether (DME)/air turbulent mixtures, Combust. Flame 162 (3) (2015) 688–702.

[30] A. Krisman, E.R. Hawkes, J.H. Chen, A parametric study of ignition dynamics at ECN spray a thermochemical conditions using 2D DNS, Proc. Combust. Inst. 37 (4) (2019) 4787–4795.

[31] G. Borghesi, A. Krisman, T. Lu, J.H. Chen, Direct numerical simulation of a temporally evolving air/*n*-dodecane jet at low-temperature diesel-relevant conditions, Combust. Flame 195 (2018) 183–202.

[32] F. Tagliante, T. Poinsot, L.M. Pickett, P. Pepiot, L.M. Malbec, G. Bruneaux, C. Angelberger, A conceptual model of the flame stabilization mechanisms for a lifted diesel-type flame based on direct numerical simulation and experiments, Combust. Flame 201 (2019) 65–77.

[33] A. Krisman, E.R. Hawkes, M. Talei, A. Bhagatwala, J.H. Chen, Polybrachial structures in dimethyl ether edge-flames at negative temperature coefficient conditions, Proc. Combust. Inst. 35 (1) (2015) 999–1006.

[34] A. Krisman, E.R. Hawkes, M. Talei, A. Bhagatwala, J.H. Chen, A direct numerical simulation of cool-flame affected autoignition in diesel engine-relevant conditions, Proc. Combust. Inst. 36 (3) (2017) 3567–3575.

[35] J.H. Chen, E.R. Hawkes, R. Sankaran, S.D. Mason, H.G. Im, Direct numerical simulation of ignition front propagation in a constant volume with temperature inhomogeneities: I. Fundamental analysis and diagnostics, Combust. Flame 145 (1) (2006) 128–144.

[36] G.H. Yu, M.B. Luong, S.H. Chung, C.S. Yoo, Ignition characteristics of a temporally evolving n-heptane jet in an iso-octane/air stream under RCCI combustion-relevant conditions, Combust. Flame 208 (2019) 299–312.

[37] S. Mukhopadhyay, J. Abraham, Influence of compositional stratification on autoignition in *n*-heptane/air mixtures, Combust. Flame 158 (6) (2011) 1064–1075.

[38] D.K. Dalakoti, B. Savard, E.R. Hawkes, A. Wehrfritz, H. Wang, M.S. Day, J.B. Bell, Direct numerical simulation of a spatially developing *n*-dodecane jet flame under spray a thermochemical conditions: Flame structure and stabilisation mechanism, Combust. Flame 217 (2020) 57–76.

[39] X. Shi, J.-Y. Chen, Y. Chen, Laminar flame speeds of stratified methane, propane, and *n*-heptane flames, Combust. Flame 176 (2017) 38–47.

[40] X. Shi, J.-Y. Chen, Z. Chen, Numerical study of laminar flame speed of fuel-stratified hydrogen/air flames, Combust. Flame 163 (2016) 394–405.

[41] X. Shi, J.-Y. Chen, Numerical analysis and model development for laminar flame speed of stratified methane/air mixtures, Combust. Flame 184 (2017) 233–245.

[42] Y. Wang, W. Han, T. Zirwes, F. Zhang, H. Bockhorn, Z. Chen, Effects of low-temperature chemical reactions on ignition kernel development and flame propagation in a DME-air mixing layer, Proc. Comb. Inst. 39 (2023) 1515–1524.

[43] C. Pantano, Direct simulation of non-premixed flame extinction in a methane–air jet with reduced chemistry, J. Fluid Mech. 514 (2004) 231–270.

[44] P. Sripakagorn, S. Mitarai, G. Kosály, H. Pitsch, Extinction and reignition in a diffusion flame: a direct numerical simulation study, J. Fluid Mech. 518 (2004) 231–259.

[45] E.R. Hawkes, R. Sankaran, J.H. Chen, A study of extinction and reignition dynamics in syngas jet flames using terascale direct numerical simulations: sensitivity to the choice of reacting scalar, Proc. Aust. Combust. Symp. (1) (2007).

[46] S. Karami, E.R. Hawkes, M. Talei, J.H. Chen, Mechanisms of flame stabilisation at low lifted height in a turbulent lifted slot-jet flame, J. Fluid Mech. 777 (2015) 633–689.

[47] S.H. Chung, Stabilization, propagation and instability of tribrachial triple flames, Proc. Combust. Inst. 31 (1) (2007) 877–892.

[48] B. Shields, J.B. Freund, C. Pantano, Stationary edge flames in a wedge with hydrodynamic variable-density interaction, Combust. Flame 211 (2020) 347–361.

[49] S. Deng, P. Zhao, M.E. Mueller, C.K. Law, Autoignition-affected stabilization of laminar nonpremixed DME/air coflow flames, Combust. Flame 162 (9) (2015) 3437–3445.

[50] S. Karami, E.R. Hawkes, M. Talei, J.H. Chen, Edge flame structure in a turbulent lifted flame: A direct numerical simulation study, Combust. Flame 169 (2016) 110–128.

[51] G. Zhai, S. Xing, A. Srna, A. Wehrfritz, S. Kook, E.R. Hawkes, Q.N. Chan, Ignition and flame stabilisation of primary reference fuel sprays at engine-relevant conditions, Combust. Flame 233 (2021) 111620.

[52] M.B. Luong, Z. Luo, T. Lu, S.H. Chung, C.S. Yoo, Direct numerical simulations of the ignition of lean primary reference fuel/air mixtures with temperature inhomogeneities, Combust. Flame 160 (10) (2013) 2038–2047.

[53] J.H. Chen, A. Choudhary, B.d. Supinski, M. DeVries, E.R. Hawkes, S. Klasky, W.K. Liao, K.L. Ma, J. Mellor-Crummey, N. Podhorszki, R. Sankaran, S. Shende, C.S. Yoo, Terascale direct numerical simulations of turbulent combustion using S3D, Comput. Sci. Discov. 2 (2009) 015001–015032.

[54] C.A. Kennedy, M.H. Carpenter, Several new numerical methods for compressible shear-layer simulations, Appl. Numer. Math. 14 (4) (1994) 397–433.

[55] C.A. Kennedy, A. Gruber, Reduced aliasing formulations of the convective terms within the Navier–Stokes equations for a compressible fluid, J. Comput. Phys. 227 (3) (2008) 1676–1700.

[56] C.A. Kennedy, M.H. Carpenter, R.M. Lewis, Low-storage, explicit Runge–Kutta schemes for the compressible Navier–Stokes equations, Appl. Numer. Math. 35 (3) (2000) 177–219.

[57] H. Tummalapalli, E.R. Hawkes, B. Savard, J.-W. Park, T. Lu, Flame stabilisation in a highly-lifted premixed jet flame in a hot cross flow, Proc. Combust. Inst. 40 (1) (2024) 105452.

[58] R.W. Bilger, The structure of turbulent nonpremixed flames, Symp. (Int.) Combust. 22 (1) (1989) 475–488.

[59] A. Krisman, E.R. Hawkes, J.H. Chen, The structure and propagation of laminar flames under autoignitive conditions, Combust. Flame 188 (2018) 399–411.

[60] T. Zhang, Y. Ju, Structures and propagation speeds of autoignition-assisted premixed *n*-heptane/air cool and warm flames at elevated temperatures and pressures, Combust. Flame 211 (2020) 8–17.

[61] D. Goodwin, H. Moffat, R. Speth, Cantera: An object-oriented software toolkit for chemical kinetics, thermodynamics, and transport processes, 2023, URL http://www.cantera.org.

[62] A. Scholtissek, W.L. Chan, H. Xu, F. Hunger, H. Kolla, J.H. Chen, M. Ihme, C. Hasse, A multi-scale asymptotic scaling and regime analysis of flamelet equations including tangential diffusion effects for laminar and turbulent flames, Combust. Flame 162 (4) (2015-04-01) 1507–1529.

[63] W.L. Chan, M. Ihme, Flamelet regime characterization for non-premixed turbulent combustion simulations, Combust. Flame 186 (2017) 220–235.

[64] N. Peters, Turbulent Combustion, in: Cambridge Monographs on Mechanics, Cambridge University Press, Cambridge, 2000.

[65] T. Echekki, J.H. Chen, Analysis of the contribution of curvature to premixed flame propagation, Combust. Flame 118 (1999) 308–311.

[66] Q. Tang, H. Liu, M. Li, M. Yao, Z. Li, Study on ignition and flame development in gasoline partially premixed combustion using multiple optical diagnostics, Combust. Flame 177 (2017) 98–108.

[67] A. Krisman, E.R. Hawkes, J.H. Chen, Two-stage autoignition and edge flames in a high pressure turbulent jet, J. Fluid Mech. 824 (2017) 5–41.

[68] C.H. Gibson, W.T. Ashurst, A.R. Kerstein, Mixing of strongly diffusive passive scalars like temperature by turbulence, J. Fluid Mech. 194 (1988) 261–293.

[69] S.H. Kim, H. Pitsch, Scalar gradient and small-scale structure in turbulent premixed combustion, Phys. Fluids 19 (2007) 115104.